# MINISTRY OF TECHNOLOGY

AERONAUTICAL RESEARCH COUNCIL
REPORTS AND MEMORANDA

# The Time-Vector Method for Lateral Stability Investigations

By PROF. DR. ING. K. H. DOETSCH

# The Time-Vector Method for Lateral Stability Investigations

By PROF. DR. ING. K. H. DOETSCH*

---

---

*Summary.*

This report extends earlier work by describing the time-vector method for lateral stability investigations. Using this method, each equation of motion of an aircraft can be represented by a closed vector polygon, the shape and size of which conveys useful information about the mode of motion under consideration. A graphical method for constructing these polygons is presented and a mechanised system of vector calculators is described in detail. Because of the availability of digital computers, the main use of the method now is in the interpretation of results obtained by computers, giving improved physical insight into aircraft lateral behaviour. This application has proved to be particularly fruitful in relation to automatic control phenomena. Several examples are given.

---

## LIST OF CONTENTS

---

3

# 1. *Introduction.*

The time-vector method for aircraft stability investigations was developed more than ten years ago[1] to satisfy two essential needs concerning the stability of the oscillatory modes of motion of an aeroplane. These needs are a knowledge of the stability characteristics (period, damping, etc.) and an understanding of the physical basis of these characteristics. Numerical methods were available[2,3] to provide the former, but it was considered that many people found it difficult to obtain a sound grasp of the physics of the motion from such calculations. By retaining information concerning the phase, as well as the amplitude, of each term in the equations of motion, the time-vector method attempted to answer both questions—what and why—in one process.

During the past twelve years the principles of the time-vector method have been expounded in the R.A.E.[1] and elsewhere[4-6]. The method has been used in theoretical stability investigations[7-9] and for the analysis[10-18] and illustration[19-21] of flight test results. Both the basic theory and the application of the method of longitudinal motion were described in detail in Ref. 1, but the value of the method when applied to lateral stability has been only briefly indicated[4,7]. The present report is intended to complete the detailed account begun in Ref. 1 by dealing with lateral stability investigations, including some effects of automatic control. A particular feature of this report is a description of some specially designed calculators: many of the original ideas involved in their design were contributed by W. J. G. Pinsker of Aerodynamics Department.

The basic idea of the time-vector method is that a periodically varying quantity can be represented by a line, of appropriate magnitude and phase, which rotates at constant angular velocity. Such lines are called time vectors and may be manipulated according to the standard rules of vector analysis. It was necessary, in Ref. 1, to extend the theory for constant amplitude oscillations to apply to oscillations with damping, as in aircraft motion, where the amplitude of each quantity varies exponentially with time.

Attention can be fixed on any particular oscillatory mode, and the excitation of each variable in this mode expressed in terms of the amplitude and phase at some arbitrary moment. Thus each variable, and hence each term in an equation of motion, can be interpreted as a vector whose magnitude, or modulus, is equal to the appropriate complex amplitude, and whose direction is at an angle equal to the phase angle. The important results for the practical use of the time-vector method is that an equation, stating that the sum of certain terms is zero, may be represented by a closed vector polygon, the sides of which stand for the individual terms. In the present application there is thus one polygon for each equation of motion, and a separate set of polygons for each oscillatory mode of the system. The shapes and relative sizes of the polygons for one mode are determined by the damping, frequency and amplitude ratios of that mode, and *vice versa.*

Throughout this report it is assumed that the stability derivatives are known and that the characteristics of the motion are required. The reverse process, of finding the derivatives once the period, damping, amplitude ratio and phase angles have been obtained from flight tests, is not considered here. This task is one to which the time-vector method is well suited; Ref. 13 is a good example of such an application.

Starting from a knowledge of the derivatives, two ways of constructing the time-vector diagrams will be described: a graphical method and a process using specially developed calculators. Considerable emphasis will be placed on the interpretation of the time-vector diagrams, by including a variety of examples.

Several examples are given because the characteristics of the lateral oscillation vary much more widely with aircraft geometry than those of the longitudinal modes. The lateral oscillation ranges from the nearly exclusively directional oscillation as found on many aircraft with straight wings of large span, to an almost pure oscillation about an axis roughly aligned with the longitudinal body axis, as for slender wing aircraft. Certain features of the motion connected with particular shape parameters of the aircraft can be discerned and will be demonstrated.

The time-vector method can be used in aircraft stability work for two purposes: as a method of analysis or as a means of representation of results. Both purposes will be considered in this report, but it seems that the most fruitful future application of the method will be to assist in the understanding and interpretation of results.

## 2. Theoretical Background.

### 2.1. Recapitulation of the Principles of the Time-Vector Method.

The time-vector method[1] is concerned with second-order oscillatory systems, a mechanical version of which, in the form of a spring-mass-dashpot system, is illustrated in Fig. 1a. The differential equation governing the motion is

$$- m\ddot{x} - k\dot{x} - cx = 0,$$  (1)

which has the general solution

$$x = x_1 e^{-t/t_D} \cos(\omega t + \varepsilon_x)$$  (2)

where $x_1$ and $\varepsilon_x$ are constants which depend on the initial conditions. $\varepsilon_x$ is the phase of $x$ relative to some datum line and is measured positive in an anti-clockwise sense. The coefficients in equations (1) and (2) are related by

$$\frac{1}{t_D} = \frac{k}{2m}$$  (3)

$$\omega^2 + \frac{1}{t_D^2} = \frac{c}{m} = \omega_0^2$$  (4)

$t_D$ is the damping time during which the amplitude of the oscillation decreases to $1/e = 0.368$ of its original value, and $\omega_0$ is the undamped natural frequency of the system. The relationship (4) can be represented as in the diagram.



$$\tan \varepsilon_D = \frac{1}{\omega t_D}$$

$$\frac{1}{t_D} = \omega_0 \sin \varepsilon_D \Bigg\}$$  (5)

$$\omega = \omega_0 \cos \varepsilon_D$$
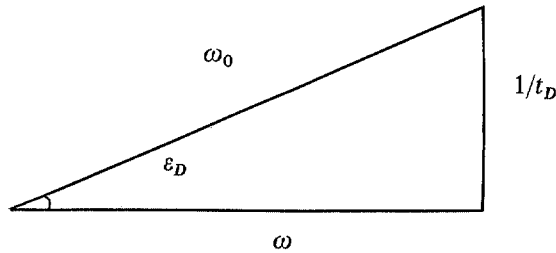
The angle $\varepsilon_D$, called the damping angle, is a measure of the relative damping of the system, which can be expressed by

$$\text{Logarithmic decrement } \delta = 2\pi \tan \varepsilon_D.$$

The basic principles of the time-vector method is that a quantity such as $x$, which has the damped harmonic time history illustrated in Fig. 1b, can be represented by a generating 'time-vector', $\bar{x}$, rotating

5

at constant angular velocity, $\omega$, in the phase plane $R$–$I$ (strictly the complex plane). Its length decreases exponentially with time. Thus its tip traces a logarithmic spiral (Fig. 1c) and the projection of this time vector on the real axis $R$ (assumed to be vertical here) produces the time-history indicated in Fig. 1b.

In the particular case of Fig. 1a the mass is assumed displaced from equilibrium by an amount $x_0$ and released from this position at time $t = 0$. Since the velocity $\dot{x}$ is zero at the instant of release, the corresponding time vector $\bar{\dot{x}}$ must be perpendicular to the real axis in order to give zero projection on this axis. If the mass is released from rest its displacement at $t = 0$ must be a maximum, which occurs when the tangent to the spiral is parallel to the $I$-axis. For any logarithmic spiral the angle between the tangent and the line normal to the radius vector is a constant, the spiral angle. Therefore if the tangent at $t = 0$ is horizontal the radius vector must be displaced from the vertical by this spiral angle, which is in fact equal to $\varepsilon_D$, the damping angle of the system under consideration. Thus the phase angle between the $\bar{x}$ and $\bar{\dot{x}}$ time vectors at $t = 0$ is $90° + \varepsilon_D$ and the length of the displacement vector at $t = 0$ is

$$\left| \bar{x}_0 \right| = x_0 \sec \varepsilon_D .$$

Equation (2) may be rewritten for these conditions, i.e. starting at $t = 0$ from maximum deflection (phase reference is the real axis):

$$x = \left| \bar{x}_0 \right| e^{-t/t_D} \cos (\omega t - \varepsilon_D) . \tag{6}$$

From this the velocity may be derived by differentiation:

$$\dot{x} = \left| \bar{x}_0 \right| e^{-t/t_D} \left[ -\frac{1}{t_D} \cos (\omega t - \varepsilon_D) - \omega \sin (\omega t - \varepsilon_D) \right]$$

and with the relations (5)

$$\dot{x} = -\omega_0 \left| \bar{x}_0 \right| e^{-t/t_D} \sin \omega t$$

$$= \omega_0 \left| \bar{x}_0 \right| e^{-t/t_D} \cos (\omega t + \tfrac{1}{2}\pi) \tag{7}$$

which confirms the phase relation between $\bar{x}$ and $\bar{\dot{x}}$ previously arrived at by qualitative geometrical argument. The length of the time vector representing $\dot{x}$ is $\omega_0$ times that of the time vector for $x$. Similarly

$$\ddot{x} = -\omega_0^2 \left| \bar{x}_0 \right| e^{-t/t_D} \cos (\omega t + \varepsilon_D)$$

$$= \omega_0^2 \left| \bar{x}_0 \right| e^{-t/t_D} \cos (\omega t + \pi + \varepsilon_D) . \tag{8}$$

Thus the acceleration and the length of its representative time vector is $\omega_0$ times that of the velocity, and $\ddot{x}$ is advanced in phase by another $(90° + \varepsilon_D)$. Thus $\dot{x}$ and $\ddot{x}$ can be represented by time vectors rotating at the same angular velocity as $x$. These relations are illustrated in Fig. 2a, together with time histories of the three variables in Fig. 2b.

Although, in the derivation of phase relationships from Fig. 1, a particular instant of time ($t = 0$) was considered, the analysis has demonstrated that the deductions are generally valid. This is because the decay factor $e^{-t/t_D}$ is common to each variable and merely indicates that each vector shrinks at the same rate. Since the time vectors rotate at the same angular velocity and shrink at the same rate, they are invariant with respect to each other and it suffices to consider their relationship to any particular instant of time, e.g. at $t = 0$.

When dealing with the equations of motion it is convenient to separate the amplitude and phase of each term. For example, equation (1) may be tabulated

6

| Modulus | $m\,\omega_0^2\,x_1$ | $k\,\omega_0\,x_1$ | $c x_1$ |
|---------|------------------|------------------|---------|
| Phase | $-\ddot{x}$ | $-\dot{x}$ | $-\bar{x}$ |

$$= 0.$$

The '$= 0$' indicates that the vectors form a closed polygon. Phase expressed as '$-\bar{x}$' means in counterphase to the $x$-vector, which may be drawn in any convenient position and with any convenient size (e.g. $x_1 = 10$). Phase '$-\dot{x}$' then means in counterphase to the $\dot{x}$ vector, which is itself advanced in phase by $(90° + \varepsilon_D)$ on $\bar{x}$. This convention of expressing phase and counterphase forces the operator to determine the appropriate phase from physical considerations rather than rely on having observed the signs correctly throughout the evaluation of the moduli.

The equilibrium of the forces of equation (1) is then represented geometrically by an isosceles triangle (Fig. 2d), the sides of which have lengths proportional to the quantities which they represent. This triangle has two useful properties: the apex angle is twice the damping angle and the height is proportional to the damped frequency (*see* diagram on page 7). For a system with several degrees of freedom, it is still possible to identify an equivalent isosceles triangle. This is of value because of the way in which the triangle summarises the basic stability characteristics of period and damping.

### 2.2. *Equations of Motion.*

The usual linearised equations of motion are used, with some modifications.

Firstly, the sideslip angle is different from the usual definition, in that positive sideslip angle is chosen to be in the same sense as positive rotation about the $z$-axis, Fig. 3.

A bar is put under the symbol, to make this clear. Thus

$$\underline{\beta} = -v/V_e = -\hat{v}.$$

In flight, particularly in the lateral oscillation which is the main theme of this report, the actual sideslip occurs as a consequence of a rotary disturbance rather than an acceleration of the cg along the $y$-axis. Since $\underline{\beta}$ is, for this particular mode, closely approximated, in magnitude as well as phase, by the deflection in azimuth, $\psi$, it helps the understanding of the physics of the motion when the sign convention for sideslip is chosen to agree with that of $\psi$.

Secondly, the acceleration along the $y$-axis is written in terms of the angle of track $\chi$.

$$\chi = \psi - \underline{\beta} \sec \gamma_e. \tag{9}$$

When referred to aerodynamic-body axes and with controls fixed, the linearised non-dimensional equations of motion for a datum flight condition which is steady, straight and *level* are

$$-A\,\ddot{\phi} + E\,\ddot{\psi} + L_\beta\,\underline{\beta} + L_\psi\,\psi + L_\phi\,\phi \qquad = 0 \tag{10}$$

$$-C\,\ddot{\psi} + E\,\ddot{\phi} + N_\beta\,\underline{\beta} + N_\psi\,\psi + N_\phi\,\phi \qquad = 0 \tag{11}$$

$$-m\,V_e\,\dot{\chi} + \qquad Y_\beta\,\underline{\beta} + Y_\psi\,\psi + Y_\phi\,\phi + W\,\phi = 0 \tag{12}$$

where

$$\psi = \dot{\chi} + \underline{\beta} = r \tag{9a}$$

$$\dot{\phi} = p.$$

For the datum condition assumed here of steady, straight and level flight and for aerodynamic-body axes it is reasonable to equate $L_\phi$ with $L_p$, $L_\psi$ with $L_r$ etc., but it is important to note that, in general, $L_\phi$ is

not the same as $L_p$ (*see* Section 22 of Hopkin[22]). However, taking $L_{\dot{\phi}} = L_p$ and similarly for other derivatives these equations can be made non-dimensional in the usual way[23], leading to

$$-\ddot{\phi}\,\hat{t}^2 + \frac{i_E}{i_A}\ddot{\psi}\,\hat{t}^2 - \frac{\mu_2 l_v}{i_A}\beta + \frac{l_r}{i_A}\dot{\psi}\,\hat{t} + \frac{l_p}{i_A}\dot{\phi}\,\hat{t} = 0 \qquad (10a)$$

$$-\ddot{\psi}\,\hat{t}^2 + \frac{i_E}{i_C}\ddot{\phi}\,\hat{t}^2 - \frac{\mu_2 n_v}{i_C}\beta + \frac{n_r}{i_C}\dot{\psi}\,\hat{t} + \frac{n_p}{i_C}\dot{\phi}\,\hat{t} = 0 \qquad (11a)$$

$$-\dot{\chi}\,\hat{t} - y_r\beta + \frac{y_r}{\mu_2}\dot{\psi}\,\hat{t} + \frac{y_p}{\mu_2}\dot{\phi}\,\hat{t} + \tfrac{1}{2}C_L\phi = 0. \qquad (12a)$$

In most of the following sections, $y_p$ and $y_r$ are neglected. The sideforce calculator (*see* Section 3.3.2) does provide, however, for a non-zero value of $y_p$, and $y_r$ can also be allowed for.

### 2.3. *The Equations of Motion Rewritten for the Vector Method.*

As mentioned in Section 2.1, the linearised differential equations of motion can be rewritten for the vector method by splitting each term into amplitude and phase. The amplitudes are obtained by substituting for each order of time derivative the corresponding power of $\omega_0$. This angular frequency can then be combined with the time-scale factor $\hat{t}$ to form the normalised angular frequency $\hat{\omega}_0$, measured in radians per airsecond.

$$\omega_0\,\hat{t} = \hat{\omega}_0.$$

In deriving the phase of each term in the vector equations, it is assumed that each derivative and inertia constant has its 'conventional' sign:

$$y_v,\, y_p,\, l_v,\, l_p,\, n_p,\, n_r,\, i_E \quad \text{negative}$$

$$y_r,\, n_v,\, l_r,\, i_A,\, i_C \qquad \text{positive}.$$

If any derivative is opposite in sign to that assumed, then the phase of the term must be reversed.

| Modulus | $\hat{\omega}_0^2\,\phi$ | $\dfrac{i_E}{i_A}\omega_0^2\,\psi$ | $\dfrac{l_v}{i_A}\mu_2\,\beta$ | $\dfrac{l_r}{i_A}\hat{\omega}_0\,\psi$ | $\dfrac{l_p}{i_A}\hat{\omega}_0\,\phi$ | $= 0$ |
|---|---|---|---|---|---|---|
| Phase | $-\ddot{\phi}$ | $-\ddot{\psi}$ | $+\beta$ | $+\dot{\psi}$ | $-\dot{\phi}$ | |

$$(13)$$

| Modulus | $\hat{\omega}_0^2\,\psi$ | $\dfrac{i_E}{i_C}\hat{\omega}_0^2\,\phi$ | $\dfrac{n_v}{i_C}\mu_2\,\beta$ | $\dfrac{n_r}{i_C}\hat{\omega}_0\,\psi$ | $\dfrac{n_p}{i_C}\hat{\omega}_0\,\phi$ | $= 0$ |
|---|---|---|---|---|---|---|
| Phase | $-\ddot{\psi}$ | $-\ddot{\phi}$ | $-\beta$ | $-\dot{\psi}$ | $-\dot{\phi}$ | |

$$(14)$$

| Modulus | $\hat{\omega}_0\,\chi$ | $y_v\,\beta$ | $\dfrac{y_r}{\mu_2}\hat{\omega}_0\,\psi$ | $\dfrac{y_p}{\mu_2}\hat{\omega}_0\,\phi$ | $\dfrac{C_L}{2}\,\phi$ | $= 0$ |
|---|---|---|---|---|---|---|
| Phase | $-\dot{\chi}$ | $+\beta$ | $+\dot{\psi}$ | $-\dot{\phi}$ | $+\phi$ | |

$$(15)$$

and the kinematic relation:
$$\left|\frac{\hat{\omega}_0\,\psi}{\dot{\psi}}\right| = \left|\frac{\hat{\omega}_0\,\beta}{\dot{\beta}}\,\frac{\hat{\omega}\,\chi}{\dot{\chi}}\right|. \qquad (16)$$

A set of polygons, representing a typical example, is shown in Fig. 4, in order to demonstrate their shape. Fig. 4 contains the rolling-moment diagram (a), the sideforce diagram (b) which is usually amalgamated

8

with the kinematic relation (c), and the yawing-moment diagram (d). The equivalent isosceles triangle is shown shaded as part of the yawing-moment polygon.

### 3. Construction of the Time-Vector Polygons for an Aircraft without Automatic Control.

#### 3.1. Introduction.

3.1.1. *General remarks.* An iterative graphical method to construct the polygons has been devised using the principles established in Ref. 1 for the phugoid motion. To speed up this process for frequent use, it has been mechanised by the design of special calculators. These two methods will be described in this section, after a few preliminary remarks which are relevant to both.

3.1.2. *Remarks on notation.* A variable such as $\phi$ is described by the time vector $\bar{\phi}$, the length of which at the datum time is the modulus $|\bar{\phi}|$. The phase angle of this vector at that time is $\varepsilon_\phi$ relative to some reference vector, which is usually taken as the sideslip vector $\bar{\beta}$. In general only the relative amplitudes of each variable are of interest, not the absolute values. Thus the value of $\dfrac{|\bar{\phi}|}{|\bar{\beta}|}$ may be required. This is a clumsy notation, and such an amplitude ratio will usually be written $\dfrac{\phi}{\beta}$, with the modulus of each vector implied but not written.

3.1.3. *Starting conditions.* Since the oscillation is usually poorly damped, it is sufficient to assume initially that the damping is zero.

$$\varepsilon_D = 0.$$

A useful approximation to the undamped natural frequency $\hat{\omega}_0$ is[24]

$$\hat{\omega}_0^2 = \frac{\mu_2 \, n_v}{i_C} + \frac{\mu_2 \, l_v}{i_A} \frac{i_E}{i_C}. \tag{17}$$

In certain cases (e.g. slender aircraft at high incidence) this could be revised to[25]

$$\hat{\omega}_0^2 = \frac{\dfrac{\mu_2 \, n_v}{i_C} + \dfrac{i_E}{i_C} \dfrac{\mu_2 \, l_v}{i_A}}{1 - \dfrac{i_E^2}{i_A \, i_C}}.$$

The assumption is also made initially that sideways motion of the centre of gravity of the aircraft is zero, i.e.,

$$\chi = 0$$

which implies that

$$\psi/\beta = 1 \tag{18}$$

and

$$\varepsilon_\psi = 0. \tag{19}$$

3.1.4. *Iteration.* The basic method is an iterative one. It starts from the approximations to the natural frequency and damping of the lateral oscillation, described in Section 3.1.3, and improves these approximations with each cycle of the iteration process until the change between cycles is small enough

9

to be ignored. The order in which the polygons are taken during the iteration is important, since this determines the convergence of the process.

For most aircraft with a moderate Dutch-roll ratio, the yawing moment polygon is the fundamental polygon in which the equivalent isosceles triangle can be found. This diagram must therefore be last, since it provides the corrections to the frequency and damping for the next cycle. As the rolling-moment polygon is relatively insensitive to changes in damping angle, it is used first. The diagrams are therefore used in the order: rolling moment, sideforce, yawing moment; although occasional extreme examples may involve iteration difficulties and require the reverse order.

Thus the procedure, which will be dealt with in more detail in Sections 3.2 and 3.3, is as follows. The rolling-moment diagram is used first, with the assumptions of Section 3.1.3. This diagram yields initial values of the amplitude ratio $\phi/\beta$, and of $\varepsilon_{\ddot{\phi}}$, the phase angle of $\ddot{\phi}$ relative to $\beta$. The phase angle of $\phi$ is then found from

$$\varepsilon_{\phi} = \varepsilon_{\ddot{\phi}} - (180 + 2\varepsilon_D).$$

This additional information enables the sideforce diagram to be drawn, from which the amplitude ratio $\psi/\beta$ and the phase angle $\varepsilon_{\psi}$ are obtained. Finally the yawing-moment diagram produces a correction factor for the undamped natural frequency $\hat{\omega}_0$ and a revised value for the damping angle $\varepsilon_D$. The whole process is then repeated.

3.1.5. *Choice of reference length.* When constructing the diagrams it is convenient to take the main vector in each polygon as the reference length. To do so has advantages in both the graphical and mechanised methods. In each polygon one vector will then be of constant length, while the others will be reduced to reasonably uniform values.

No single reason governs the choice of reference length. In the yawing-moment polygon the yaw inertia term $\hat{\omega}_0^2 \psi$ is chosen because it contains the highest power in $\hat{\omega}_0$. The change in overall dimensions of the diagram will therefore be minimised at each iteration.

When all other terms in the equation are divided by this reference length, they can be written solely in terms of amplitude ratios. For example

$$\frac{n_p}{i_C} \hat{\omega}_0 |\bar{\phi}| \div \hat{\omega}_0^2 |\bar{\psi}| = \frac{n_p}{i_C} \frac{1}{\hat{\omega}_0} \frac{\phi}{\psi}.$$

From a comparison of the sideforce equation (15) with the kinematic equation (16) it is clear that by eliminating the $\hat{\omega}_0 \chi$ term, both equations can be represented in a single diagram or on a single mechanical calculator. Since the longest vector will usually be that representing $\beta$ (Fig. 4) the choice of this vector as reference will immediately make the length of the other long vector represent the important amplitude ratio $\dfrac{\psi}{\beta} = \dfrac{\psi}{\beta}$.

In the rolling-moment diagram the sideslip term is selected as reference length because $\dfrac{\mu_2 l_v}{i_A} \beta$ will usually be the longest of the 'excitation' vectors.

3.2. *Graphical Method.*

3.2.1. *Rolling-moment polygon.* Expression (13) may be rewritten with the amplitude of each term divided by the reference length $\dfrac{\mu_2 l_v}{i_A} \beta$ and with the order of the terms rearranged as they occur in the graphical process.

| Modulus | 1 | $\dfrac{l_r}{\mu_2 l_v}\dot\omega_0\dfrac{\psi}{\beta}$ | $\dfrac{i_E}{\mu_2 l_v}\dot\omega_0^2\dfrac{\psi}{\beta}$ | $\dfrac{l_p}{\mu_2 l_v}\dot\omega_0\dfrac{\phi}{\beta}$ | $\dfrac{i_A\dot\omega_0^2}{\mu_2 l_v}\dfrac{\phi}{\beta}$ | |
|---|---|---|---|---|---|---|
| Phase | $+\bar\beta$ | $+\dot\psi$ | $-\ddot\psi$ | $-\dot\phi$ | $-\ddot\phi$ | $=0.$ |

$$(20)$$

A working sheet has been prepared (Table 1) which has separate spaces for the amplitude and direction of each term.

If the derivatives for a particular aeroplane are given, the first two columns of the working sheet may be filled in. All phase angles are measured relative to $\beta$, which is drawn in the positive abscissa direction (Fig. 5a). By equation (19), $\psi$ is in the same direction, so that $\dot\psi$ is at right angles to this (since $\varepsilon_D = 0$ initially). With the initial approximations, equations (17) and (18), the magnitudes of the $l_r$ and $i_E$ terms may be worked out. The unit vector is drawn in positive $\beta$ direction, the $l_r$ term is drawn at right angles to this and the $i_E$ term at right angles again (Fig. 5a). The resultant, $AB$, of these three vectors is called the roll excitation $R_E$. Since the two remaining vectors involve $\dot\phi$ and $\ddot\phi$, they will be orthogonal and will therefore meet at a point on a circular arc drawn on $R_E$ as diameter. Neither the direction nor the length of these roll impedance terms is known but since $\triangle ACB$ is a right angled triangle

$$\tan CAB = \tan\eta = \frac{BC}{CA} = \frac{l_p}{i_A\dot\omega_0} \tag{21}$$

and this *is* known. The inertia vector $AC$ may therefore be inserted at an angle $\eta$ to $R_E$ and the points $B$ and $C$ joined to give the $l_p\,p$ vector. (An alternative to constructing the semicircle on $AB$ as diameter in order to establish the point $C$ is to draw the $l_p\,p$ vector at an angle $(90-\eta)$ to $AB$. This will meet the inertia vector at $C$.)

From the diagram the length of the roll inertia vector can be measured. If this length is $R_I$

$$R_I = \frac{i_A}{\mu_2 l_v}\dot\omega_0^2\frac{\phi}{\beta}$$

or

$$\frac{\phi}{\beta} = \frac{\mu_2 l_v}{i_A}\frac{R_I}{\dot\omega_0^2}. \tag{22}$$

(In both the relations of (21) and (22), only the magnitudes of $l_p$ and $l_v$ are used, not the sign.) The phase of $\ddot\phi$, written $\varepsilon_{\ddot\phi}$, is also obtained, from which

$$\varepsilon_\phi = -(180° + 2\varepsilon_D) + \varepsilon_{\ddot\phi}.$$

3.2.2. *Sideforce polygon.* Once the phase of $\phi$ and the amplitude ratio $\dfrac{\phi}{\beta}$ have been estimated, the sideforce polygon can be constructed. The unit of length is taken to be $\dot\omega_0\beta$, so that (15) becomes, when $y_p$, $y_r$ are, as usual, neglected

| Modulus | $\dfrac{y_v}{\dot\omega_0}$ | $\dfrac{C_L}{2\dot\omega_0}\dfrac{\phi}{\beta}$ | $\dfrac{\chi}{\beta}$ | |
|---|---|---|---|---|
| Phase | $+\bar\beta$ | $+\bar\phi$ | $-\dot\chi$ | $=0.$ |

$$(23)$$

The first two terms may be drawn in (Figs. 5b, top left), since their approximate amplitudes and phases are known, and the resultant $\dot\chi$—vector obtained. Next the kinematic relation (16) may be plotted (Fig. 5b, bottom left) but it can readily be incorporated with the sideforce equation because, as previously explained, the polygon obtained from the kinematic equation has the same resultant $\dot\chi$-vector. This is shown in Fig. 5b, right. Measurement of the length $EF$ yields the amplitude ratio $\psi/\beta$ and the angle $DEF$ is the

phase angle $\varepsilon_\psi$ between the $\dot\beta$ and $\dot\psi$ vectors. From the basic time vector properties, this angle is also the angle between the $\beta$ and $\psi$ vectors. The significance of this angle will become clear when the third and final polygon is constructed.

3.2.3. *Yawing moment polygon.* All phase angles and amplitude ratios have now been estimated. Expression (14) is, when rewritten with $\dot\omega_0^2\,\psi$ as reference length:

$$
\begin{array}{c|c|c|c|c|c}
\text{Modulus} & \dfrac{\mu_2\,n_v}{i_C}\ \dfrac{1}{\dot\omega_0^2\,\psi/\beta} & \dfrac{i_E}{i_C}\ \dfrac{\phi}{\psi} & \dfrac{n_p}{i_C}\ \dfrac{1}{\dot\omega_0}\ \dfrac{\phi}{\psi} & \dfrac{n_r}{i_C\,\dot\omega_0} & 1 \\[2ex]
\hline
\text{Phase} & -\ddot\beta & -\ddot\phi & -\dot\phi & -\ddot\psi & -\ddot\psi
\end{array}
\tag{24}
$$

The $n_v$ term is drawn first (Fig. 5c), with the $i_E$ and $n_p$ terms added in succession. If the yaw-damping vector is drawn with a length $\dfrac{n_r}{i_C\,\dot\omega_0}$ in counterphase to the new $\dot\psi$ direction obtained from the sideforce polygon, the length of the closing vector $GH$ is in fact the frequency correction parameter $R_\omega$.

$$
\text{New}\,(\dot\omega_0)^2 = R_\omega \times \text{Old}\,(\dot\omega_0)^2 . \tag{25}
$$

Ultimately $GH$ will be of unit length, appropriate to the yaw inertia term. To obtain the new approximation to the damping angle, the $\psi$ vector direction $XH$ (Fig. 5c), must be drawn in by adding $\varepsilon_\psi$ from Fig. 5b to the phase of $\beta$, and then

$$
2\varepsilon_D = \lfloor XHG .
$$

In this particular example $\beta$ is leading $\psi$ ($\varepsilon_\psi$ negative), which is beneficial.

3.2.4. *Iteration.* Once the new estimates of $\dot\omega_0$ and $\varepsilon_D$ are known, the process may be repeated. Vectors representing quantities such as $\psi$ and $\dot\psi$ will now have a phase difference of $(90° + \varepsilon_D)$. In the rolling moment diagram the construction of the roll damping and inertia vectors will be slightly different.

After the first three vectors are drawn the roll excitation vector is now a chord of the auxiliary circle and not the diameter. Because $\varepsilon_D$ is no longer zero the angle subtended by this chord at the circumference is $(90° - \varepsilon_D)$. The centre of the auxiliary circle is found, therefore, by bisecting $AB$ and drawing a line at an angle $\varepsilon_D$ to $AB$, as shown in Fig. 6. Where the lines meet is the centre of the circle. For non-zero $\varepsilon_D$, the expression for the angle $\eta$ also changes, and is

$$
\tan\eta = \frac{\lambda \cos \varepsilon_D}{1 - \lambda \sin \varepsilon_D} \tag{26}
$$

where

$$
\lambda = \frac{l_p}{i_A\,\dot\omega_0}
$$

and only the magnitude of $l_p$ is used.

The roll inertia vector $R_I$ is measured again, and the iteration proceeds. After one or more iterations a sufficiently accurate set of polygons will usually be obtained. The complete process may be followed by referring to the worked example in Table 2 and the sequence of diagrams in Fig. 7. The third approximation differs so little from the second that it is not entered in the diagrams. (It was shown, incidentally, in Fig. 4.)

3.3. *Vector Calculator Method.*

A routine and rapid method to solve the equations of motion by means of simple vector calculators, instead of the more laborious graphical process, has been fully developed and used during the past two decades. The design of these calculators has now been frozen to give what is considered to be a reasonably

12

universal and quick-convergence system. It covers the range of derivatives and derivative ratios experienced by the author and others during that period, and it is hoped will be valid for some time to come.

The principle of the vector calculators is essentially the same as in the graphical method, but for ease of mechanisation some differences have been introduced. A separate working sheet has been prepared (Table 3).

There are three calculators (Figs. 9a, 10a and 11a), each of which corresponds to one of the three polygons previously described. Each calculator consists of a number of linked and pivoted linear or angular scales. (The photos show the calculators set to correspond to the first iteration of the example previously illustrated in Figs. 4 and 7.)

3.3.1. *Rolling moment calculator*. To facilitate the determination of the roll damping and inertia terms the rolling-moment polygon is split into two parts, the first comprising the 'excitation' terms and the second 'impedance' terms. Each part has its own unit of length. Fig. 8 shows what has been done.

In Fig. 8 the rolling moment polygon as obtained in the graphical process (Fig. 5a) is shown at $ADBC$. On the calculators the first part, from $A$ via $D$ to the point $B$, is the same except that for convenience the $l_r$ and $i_E$ vectors are made orthogonal (such an approximation will only introduce errors in the rare case of good Dutch-roll damping), although the $l_r$ term is not always at right angles to the unit reference vector. The triangle of the impedance vectors $ACB$ (Fig. 8) is now separated, and the vector lengths are normalised by making $AB'$ the new unit of length. Triangle $ACB$ becomes triangle $AC'B'$. $AC'$ is now a modified roll inertia term and is given the symbol $R'_I$.

To establish the exact location of $C'$ a technique different from that applied in Fig. 6 has been adopted here. It uses the important property of the triangle $AB'C'$ that

$$\frac{B'C'}{C'A} = \frac{l_p}{i_A \dot\omega_0} = \lambda$$

(where $l_p$ takes its numerical value only). Therefore the point $C'$ lies on the circumference of one of a family of circles known as Apollonius' circles. Arcs of such orthogonal circles have been constructed to give a grid for obtaining $R'_I$, given $\lambda$ and $\varepsilon_D$ (Fig. 9a). A detailed description of the rolling-moment calculator follows, and reference should be made to the annotated diagram of Fig. 9b.

This calculator consists of four parts: the baseplate $W$, a pivoting piece $X$ containing the $i_E \dot\psi$ and $l_r \dot\psi$ vectors; a second pivoting piece $Y$ with the roll excitation scale $R_E$ and the orthogonal circular arcs giving the roll damping co-ordinates; and a simple scale $Z$ representing the roll inertia vector scaled as $R'_I$. The parts $Y$ and $Z$ pivot about the same point $A$, while $X$ pivots about $D$; $AD$ represents unit distance for the first part of the polygon, as in Fig. 8. (The points $A$, $D$, $B$, $B'$, $C'$ are the same as in Fig. 8.)

To use this calculator, proceed as follows.

(1) Set the arrow $E$ at the current value of the phase angle $(\varepsilon_\psi + \varepsilon_D)$.

(2) Locate on the co-ordinate plane $X$ the point $B$ specified by the $l_r$ and $i_E$ co-ordinates on the calculator sheets (Table 3).

(3) Place the roll excitation scale, $R_E$, on this point $B$ and read off the value of $R_E$ at that point.

(4) Find on the plane $Y$ a point $C'$ specified by the co-ordinates $\varepsilon_D$ and $\dfrac{l_p}{i_A \dot\omega_0}$.

(5) Place the roll inertia scale $Z$ so that it passes through this point $C'$.

(6) Read the value of $R'_I$ at this point and also the phase angle of $\ddot\phi$ given by the intersection of the $R'_I$ scale with $\varepsilon_{\ddot\phi}$ scale.

(7) Tabulate the various readings on the special sheet and make any subsidiary calculations before going on.

(In cases with extremely large values of $i_E$, the errors, mentioned above, associated with making the $i_E \dot\psi$ and $l_r \dot\psi$ terms orthogonal, may be reduced by aligning the product of inertia term correctly (i.e. setting $(\varepsilon_\psi + 2\varepsilon_D)$ on the calculator), as shown in Fig. 9c, interchanging the $l_r$ and $i_E$ terms in the co-ordinate plane.)

13

3.3.2. *Sideforce calculator.* The sideforce calculator (Figs. 10a and 10b) repeats exactly the graphical process and consists of five parts. A baseplate $F$ contains two pivot points $H$ and $P$ which are unit distance apart to represent the $\beta$ vector. A channel $G$, pivoting about $H$, carries the slide $J$, which contains a third pivot point $K$. The distance $HK$ represents the $y_v\,\beta$ vector, which is set by the mark $M$ against the $y_v$ scale on $G$. Pivoting about $K$ is a grid $L$ for setting the values of the $y_p\,\dot\phi$ and $C_L\,\phi$ vectors. For simplicity it is assumed that $\phi$ and $\dot\phi$ are at right angles, which is true, of course, only for very small damping. Since the $y_p$ term is rarely of much importance, this approximation is justified. The final scale $N$ pivoting about $P$ represents the $\dot\psi$ vector and enables the amplitude ratio $\dot\psi/\beta$ and the phase angle $\varepsilon_\psi$ to be read directly. To use the sideforce calculator:

(1) Set the value of $\varepsilon_D$ by means of the angular scale on $G$.

(2) Slide $J$ along until the mark $M$ is against the appropriate value of $\dfrac{y_v}{\dot\omega_0}$ on $G$.

(3) Turn $L$ to the value of the phase angle $\varepsilon_\phi$.

(4) On the grid $L$ find the point given by the co-ordinates $\dfrac{y_p}{\mu_2}\,\dfrac{\dot\phi}{\beta}$ and $\dfrac{C_L}{2}\,\dfrac{\phi}{\beta}\,\dfrac{1}{\dot\omega_0}$ (normally $y_p$ is taken to be zero).

(5) Set the scale $N$ to pass through this point and read the value of $\dot\psi/\beta$ at that point and also the phase angle $\varepsilon_\psi$.

(6) Enter these readings on the working sheet.

It is possible to allow for $y_r$ by the following expression.

$$\left(\frac{\dot\psi}{\beta}\right)_{\text{true}} = \left(\frac{\dot\psi}{\beta}\right)_{\text{observed}} \Big/ \left(1 - \frac{y_r}{\mu_2}\right)$$

where $y_r$ takes its appropriate sign.


3.3.3. *Yawing moment calculator.* Mechanically the most complex, the yawing moment calculator has two main parts and a detachable scale, shown assembled in Fig. 11a and separated in Fig. 11b. The part $R$ slides in a channel on the part $Q$ so that the $n_v\,\beta$ vector can be set as the distance between the pivots $U$ and $W$. The main sliding member $R$ carries a rotating scale $T$, pivoted at $U$, with which the phase angle $\varepsilon_\psi$ is set and then locked with the locking screw $S$. Mounted on the scale $T$ is a four-bar linkage designed to put the $n_r\,\dot\psi$ vector $V$ at the correct phase angle $(90 + \varepsilon_D + \varepsilon_\psi)$ to the sideslip vector $UW$. This it does with good accuracy for the range of values of $\varepsilon_D$ and $\varepsilon_\psi$ covered in the calculators. The arm $V$ is longer than the distance $UY$ so that, for increasing damping, the vector $V$ rotates clockwise relative to $UX$, the unit vector (yaw inertia term). The detachable scale $D$ has a pin at $E$ which fits into a series of holes along $V$, and the other end of $D$ has a slot which slides over the pivot knob at $U$ to give a floating zero.

On the other piece, $Q$, there is a scale $Z$ which pivots about $W$ to allow the phase angle of the $\ddot\phi$ vector to be set. The scale itself represents the $i_E\,\ddot\phi$ vector. Sliding up and down the scale $Z$ is another scale $A$ for setting up the $n_p\,\dot\phi$ term.

To use this calculator:

(1) Set the phase angle $\varepsilon_\psi$ by rotating the scale $T$ and lock with the screw $S$.

(2) Slide the piece $R$ along until the mark $B$ indicates the desired value of $\dfrac{\mu_2}{i_C}\,\dfrac{n_v}{\dot\omega_0^2}\,\dfrac{1}{\dot\psi/\beta}$. (The four-bar linkage with $V$ is best kept out of the way at this stage.)

(3) Set the phase angle $\varepsilon_{\ddot\phi}$ by rotating the arm $Z$.

(4) Slide the scale $A$ down the arm $Z$ to the appropriate value of $\dfrac{i_E}{i_C}\,\dfrac{\ddot\phi}{\dot\psi}$.

(5) Locate on $A$ a point defined by the value of $\dfrac{n_p}{i_C}\,\dfrac{\dot\phi}{\dot\psi}\,\dfrac{1}{\dot\omega_0}$ and the current value of the damping angle $\varepsilon_D$.

14

(6) Insert the pin, on the detachable scale $D$, in the hole on the scale $V$ given by the value of $\dfrac{n_r}{i_c}\dfrac{1}{\hat{\omega}_0}$.

(7) With the pivot knob $U$ in the slot in $D$, rotate the linkage $UV$ and the scale $D$ until the point located in step 5 lies on the axis of the scale $D$.

(8) Read the value of $R_\omega$ at this point and the corrected damping angle where the unit arm $UX$ intersects the $\varepsilon_D$ scale. (A concentric scale enables the damping to be read in terms of logarithmic decrement.)

From $R_\omega$ a new value for the undamped frequency, $\hat{\omega}_0$, is calculated and used, with the corrected damping angle, for the next iteration.

### 4. Examples.

Four aircraft, ranging from a straight wing, high aspect ratio type to a slender-wing aircraft of low aspect ratio, are used to illustrate the variety of lateral oscillation characteristics that can occur in practice.

#### 4.1. High Aspect Ratio, Straight Wing Aircraft.

Typical of many aircraft in widespread service throughout the world, this type has a cylindrical fuselage and a straight wing, of aspect ratio 9, which carries the engines. The longitudinal principal axis of inertia is closely aligned with the fuselage datum, and the yaw and roll inertias do not differ by much more than a factor 2.

Fig. 12 shows the variation with lift coefficient of the main lateral derivatives. Important points to note are that $-l_v$ is small and decreases in magnitude with increasing $C_L$ while $n_v$ is bigger and increases; the damping in roll, $-l_p$, is very large and $-\dfrac{l_p}{i_A} \simeq 7$; the cross coupling term $l_r$ increases rapidly with $C_L$ and reaches a large value at high $C_L$; the product of inertia $i_E$ is very small. The yaw damping derivative, $-n_r$, is constant at about 0·08 and $-\dfrac{n_r}{i_C} \simeq 0\cdot8$.

The general effect of these derivatives may be seen in Fig. 13. All these results were obtained by using the mechanical vector calculators, each calculated point taking about 20 minutes calculating time. Over the $C_L$ range the changes in the various parameters are small. The damping is always at a high level (for the lateral oscillation) and the Dutch-roll ratio $p/r$ is very low, indicating that the motion is primarily in yaw. Instead of the period, $P$, of the oscillation the product of period and indicated airspeed (more correctly EAS ft/sec) is plotted because this 'indicated wavelength' varies far less from one aircraft type to another or, generally, as a function of speed and altitude. It will also become obvious, with subsequent examples, that abnormal behaviour can more readily be recognised and discussed.

Vector polygons for $C_L = 0\cdot8$ at sea level are shown in Fig. 14. In the rolling-moment polygon, the most important terms are those due to rate of yaw and rate of roll: they both contribute to a very early phase of the roll acceleration vector $A\ddot{\phi}$. This has beneficial results in the sideforce polygon, where the phase of the $\phi$ term is such as to aid slightly the $Y_\beta\beta$ vector in producing a favourable phase angle $\varepsilon_\psi$ between the $\dot{\beta}$ and $\dot{\psi}$ vectors. The apex angle of the equivalent isosceles triangle, shown in the yawing-moment diagram, is thereby increased. The yawing-moment diagram also shows that the main stiffness is due to $N_\beta$ and the main damping is due to $N_\psi\, (= N_r)$. Both the $N_\phi$ and product of inertia vectors are sufficiently small to be neglected. Finally, the vector star of the parameters of motion shows how closely $\psi$ equals $\beta$, thus justifying the initial assumption of equation (18).

#### 4.2. Delta Wing Aircraft of Small Span.

Compared with the previous example, certain important derivatives now vary quite noticeably as $C_L$ changes (see Fig. 15). This is a consequence of both the sweep effect and the small aspect ratio of 1·8. In particular, $-l_v$ increases from just over 0·01 to nearly 0·09 as $C_L$ increases from 0 to 0·6, while $-y_v$ decreases sharply at high $C_L$. Because of the small span, the damping in roll derivative, $-l_p$, is now small and the inertia coefficients are much larger than before; both $-\dfrac{l_p}{i_A}$ and $-\dfrac{n_r}{i_C}$ are reduced, to about 0·8 and 0·5 respectively. The product of inertia is more negative at high $C_L$.

15

The derivative variations with $C_L$ are reflected in the curves of the stability characteristics given in Fig. 16. Although the 'indicated wavelength' is still more or less constant at about 1000 ft, the damping decreases nearly to zero by a $C_L$ of 0·6, while the Dutch roll ratio $p/r$ increases from 0·5 at zero lift to a maximum of 2·65 at $C_L = 0.4$.

The factors contributing to these serious changes may be deduced from the vector diagrams in Fig. 17, drawn for $C_L = 0.6$. In the rolling-moment polygon the $L_\psi \psi$ and $L_\phi \dot\phi$ vectors are now very much smaller than before, which means that the phase of the inertia vector is so late that the bank term is the sideforce polygon is nearly in counterphase to the $Y_\beta \beta$ vector. And because the $\phi/\beta$ ratio is also large, a very unfavourable phase angle between the $\psi$ and $\beta$ vectors is produced. This phase angle is nearly sufficient to counteract the other damping terms in the yawing-moment diagram. Only very small damping remains. Neither the product of inertia term nor the $N_\phi \dot\phi$ term may now be neglected: the product of inertia contributes a significant part of the effective stiffness and the $N_\phi \dot\phi$ vector counteracts the beneficial effect of the yaw damping. This is because the yawing motion and rolling motion are nearly in counterphase, as can be seen in the vector star. Despite the considerable change in the character of the motion, compared with the previous aircraft, $\psi$ and $\beta$ still differ only slightly in magnitude and phase.

### 4.3. Swept Wing Aircraft.

This aircraft has a moderately swept wing, a high set tail fin and the engine underslung beneath the nose. (This case may also be considered typical for transport aircraft with tail loading ramp and high set tail.) An important consequence of this layout is that the longitudinal principal axis of inertia is inclined downwards at an angle of about 10° to the fuselage datum. At incidences below this value, therefore, the product of inertia is positive (see Fig. 18). Other points of note are that the yaw to roll inertia ratio is now about 5, $n_p$ is positive over a large part of the $C_L$ range because of the high tail, $-l_v$ increases to a

maximum of 0·13 at a $C_L$ of 0·7, and $-\dfrac{l_p}{i_A} \simeq 6$.

The lateral stability characteristics (Fig. 19) show some unusual features. The oscillation is unstable at high speed, i.e. low $C_L$. Increase of altitude extends the unstable region. The wavelength is rather long at low $C_L$ but becomes much smaller at higher $C_L$. The Dutch roll ratio reaches values in excess of 6 at sea level and 8 at altitude.

In order to explain these unusual characteristics, two sets of vector polygons have been chosen, one for $C_L = 0.3$, Fig. 20a, and the other for $C_L = 1.0$, Fig. 20b, both at sea level. In the first case both $i_E$ and $n_p$ are positive. This sign of the product of inertia, combined with the large Dutch-roll ratio, produces a vigorous yawing moment, $E\ddot\phi$, more or less in counterphase to the damping in yaw, $N_\psi \dot\psi$, thus causing the instability of the motion. The positive yawing moment due to rate of roll, as a consequence of the high tail, reduces the virtual spring force of the system, being largely in counterphase to $N_\beta \beta$. This has the effect of lengthening the wavelength.

In the second case, Fig. 20b, both $i_E$ and $n_p$ have changed their sign. The product of inertia vector, $E\ddot\phi$, has two effects on the equilibrium of yawing moments. Firstly it contributes nearly as much again as $N_\beta \beta$ to the virtual spring force, thus causing the frequency to go up and the wavelength to shorten, as mentioned above. The second effect is a strong additional component in phase with the damping in yaw. This creates such reserves in damping that even the extremely large unfavourable phase angle $\varepsilon_\psi$, produced by the bank term $W\phi$ as a consequence of the large Dutch-roll ratio, fails to destabilise the motion.

### 4.4. Slender-Wing Aircraft (A.R. = 1·0).

Perhaps the most unusual aircraft type considered in this report is the slender wing of unity aspect ratio, of the general shape proposed for a supersonic transport. It is called slender because the span is of the order of half the overall length.

Of the derivatives shown in Fig. 21, some have been measured and others estimated, assuming the wing area is ten times the fin area. Compared with the preceding examples, the slender-wing aircraft has many unusual features. Of particular importance are: the large yaw and small roll inertias, which, with the large incidences at low speeds, imply a very large and negative product of inertia, $i_E$; the small damping in roll

16

such that $-\dfrac{l_p}{i_A} < 1$; the very large value of $-l_v$ resulting from the high leading-edge sweepback (of the order 70°) and low aspect ratio.

The low wing loading means that the approach conditions are $C_L = 0.5$ and $\alpha = 15°$, for which $-l_v = 0.22$ and $-i_E/i_A > 1$. Fig. 21 shows $n_p$ as positive and more or less constant. This is a difficult derivative to measure or estimate, but more recent ideas[25] indicate that $n_p$ will become increasingly negative as $C_L$ increases, as a result of sidewash on the fin.

The basic stability characteristics are illustrated in Fig. 22. Vector diagrams are shown for two flight conditions in Figs. 23a and 23b. At low $C_L$, Fig. 23a, the $L_\psi \, \psi$ and $E\ddot{\psi}$ vectors in the rolling-moment diagram are small and the phase of $A\ddot{\phi}$ is late. In the sideforce diagram the late phase of $\phi$ and the large ratio $\phi/\beta$ lead to an unfavourable phase angle $\varepsilon_\psi$ between $\psi$ and $\beta$. The yawing moment diagram shows that important contributions to the effective damping are made by the $E\ddot{\phi}$ and $N_\phi \, \dot{\phi}$ vectors. (If $N_\phi$ were negative, however, as discussed above, the $N_\phi \, \dot{\phi}$ vector would reduce the effective damping.)

At $C_L = 0.5$, Fig. 23b, the inertia effects dominate the motion. The large product-of-inertia vector and small damping-in-roll vector in the rolling-moment diagram cause the phase of $A\ddot{\phi}$ to be very late. The $W\phi$ vector in the sideforce diagram is many times bigger than the $Y_\beta \, \beta$ vector, with the result that the phase angle between $\psi$ and $\beta$ is very large and detrimental. Both the product-of-inertia vector $E\ddot{\phi}$ and the yaw inertia vector $C\ddot{\psi}$ are much larger than any of the aerodynamic terms in the yawing-moment polygon. The product-of-inertia vector now contributes vigorously to the effective damping and over 70 per cent of the effective stiffness. A consequence of this is that the frequency of the Dutch-roll oscillation does not fall off with decreasing speed as would be the case with a more conventional aircraft. Low frequency or long period of oscillation would have produced much larger and perhaps intolerable Dutch-roll ratios.

An important point to note is that the rolling motion ($\phi$) and the yawing motion ($\phi$) are nearly in counterphase to each other. The phase angle $\varepsilon_{\phi\psi}$ between $\phi$ and $\psi$ has been computed over the $C_L$ range and is shown in Fig. 22. For $C_L > 0.3$, $\varepsilon_{\phi\psi} \simeq 180°$. If $\varepsilon_{\phi\psi} = 180°$, then $\psi$ is at its maximum negative value when $\phi$ is at its maximum positive value (see Fig. 24), so that the resultant angular velocity is $\Omega$ about an axis inclined at an angle of $\alpha_I + \Delta$ to the wind-body axis.

$$\Omega^2 = \dot{\phi}^2_{\max} + \dot{\psi}^2_{\max} = \dot{\phi}^2_{\max}\left(1 + \frac{1}{\phi/\psi}\right)$$

and

$$\tan(\alpha_I + \Delta) = \frac{\psi \max}{\phi \max} = \frac{1}{\phi/\psi}.$$

$\Delta$ is a small angle (see Fig. 22) so that the axis of oscillation in this case is approximately the principal axis of inertia. The aircraft cg also moves sideways to some extent, and it can be shown that the aircraft oscillates, in a pendular fashion, about an axis above and roughly parallel to the principal inertia axis.

## 5. Some Aspects of Automatic Control.

### 5.1. General Remarks.

It has been indicated that the time-vector method lends itself particularly well to the interpretation of results obtained by mathematical analysis or machine computation. This application is specially useful when considering the more complex effects of automatic control. In fact, in some cases, this has proved to be the best means of achieving a proper understanding of unexpected phenomena, when flying under automatic control[7].

The designer of automatic flight-control systems frequently uses root locus plots to gain insight into the variation of flight behaviour. These plots combine damping and frequency information in a single curve for each mode of motion, and it allows the correct transfer functions of automatic control terms to be introduced.

In many cases, however, and in particular in the early stages of control design, it suffices to describe the action of the automatic control systems in terms of individual parameters of motion (or the sum of several) with fixed coefficients. Thus the usual linear differential equations of the uncontrolled aircraft can be retained, with the simple addition of such further linear control terms. This quite common procedure makes these problems amenable to treatment also by the time-vector method.

The results of such simplified analysis can again be plotted in the root locus diagram, but often designers prefer in this case to use a 'stability diagram' as exemplified in Fig. 25 in which the real and imaginary parts of the solution, i.e. damping and frequency, are plotted separately (*see* also Ref. 3). This graph is particularly suitable for the discussion of the effect of individual control terms with linearly increasing control signal strength or 'gearing'.

### 5.2. Aileron Control.

As an example of how the time-vector method improves the insight into unusual flight behaviour with automatic control, the addition of automatic aileron control proportional to roll angle will be discussed first. When such unsophisticated aileron control was applied in an early automatic control system, the pilots complained that small settings of aileron gearing produced the unexpected effect that the roll amplitudes of the usual lateral oscillation were increased rather than suppressed. The reasons for this effect, and also for the remarkable associated effect of such control on the damping of the oscillation, were subsequently readily explained by means of the time-vector method.

The differential equation of the rolling moments (equation 10)) is augmented by the additional control term, which, with the assumed constancy of the coefficient, may be transferred to the left hand side and treated like all the other aircraft terms.

$$-A\ddot{\phi} + E\ddot{\psi} + L_\beta\,\beta + L_\psi\,\dot{\psi} + L_\phi\,\dot{\phi} + L_\xi\,F_\phi\,\phi = 0 \tag{27}$$

$F_\phi$ is the aileron gearing, i.e. degrees aileron deflection per degree bank angle. The other equations (11) and (12) may, for our present purpose, remain unaltered. The complete solution of the simultaneous differential equations is plotted in the stability diagram, Fig. 25, as a function of the aileron gearing constant, $F_\phi$.

For zero aileron gearing, the roots of the uncontrolled aircraft appear as the starting values for the development of the different modes of dynamic motions. The heavily damped roll subsidence can be recognized, and the other aperiodic motion, the spiral root, is so small that it cannot be shown distinctly near the origin of the graph.

When aileron gearing is applied, these real roots change their numerical values in an opposite sense; the damping of the roll subsidence decreases rapidly, through the introduction of a kind of 'spring force' in the roll degree of freedom by means of the automatic aileron control, and the damping of the spiral is correspondingly augmented. This is because the automatic aileron control tends to erect the aircraft in bank when the spiral motion tries to develop bank.

At a relatively low aileron gearing of about one tenth of a degree of aileron deflection per degree of bank, both aperiodic roots combine and degenerate into a single complex pair, i.e. the subsidences disappear and a new lateral oscillation begins, which may be termed 'roll oscillation' as distinct from the yaw oscillation (Dutch roll) which already exists for the uncontrolled aircraft. Initially this new roll oscillation has a very low frequency (dotted line) and is extremely well damped by comparison with the yaw oscillation, but with increasing gearing $F_\phi$ the new oscillation yields some of its damping to the yaw oscillation. (The sum total of the damping of all the aircraft modes of motion, as expressed by the coefficient of $D^3$ in the stability quartic, remains unchanged by the introduction of a pure spring force term $F_\phi$.)

It is of great interest to see how the mechanism of this exchange of damping operates. The vector method will now be used for an investigation of the phenomenon.

For this investigation a number of points along the abscissa are chosen *viz.* at aileron gearings $F_\phi = 0$, 0·05, 0·4 (where the damping of the yaw oscillation reaches a maximum) and finally at $F_\phi = 2·0$, where the interaction between the roll and the yaw oscillation has subsided. For each of these gearings the vector polygons have been established and are shown in Figs. 26–28.

18

In the rolling-moment polygon the introduction of a term proportional to $\phi$ means the insertion of a corresponding time vector roughly at right angles to the $L_\phi\,\phi$ vector (observe the change of the polygon for the values $F_\phi = 0$ and 0·05). This necessarily means first of all an opening-out of the polygon by an increase in length of *all* rolling-reaction vectors whilst the excitation, consisting in this example of the $L_\beta\,\beta$ and $L_\psi\,\psi$—vectors, remains practically unchanged. As a consequence of this relative increase of all roll-reaction vectors the Dutch-roll ratio must increase.

The maximum increase occurs at an aileron gearing of $F_\phi = 0.4$ (*see* Fig. 26), which also corresponds to the point in the stability diagram where the dotted lines of the imaginary roots cross each other, i.e. where both oscillations have the same frequency.

Beyond this point the lengths of the roll-reaction vectors decrease again and they become eventually very small indeed (*see* polygon for $F_\phi = 2$), indicating a marked reduction in the Dutch-roll ratio. The cause for this reversal of the roll-amplitude effect can be found in the phase rotation of the rolling mode in an anti-clockwise direction. This phase advance has persisted right through from very small initial values of aileron gearing (*observe* Fig. 26). At large values of $F_\phi$ this phase rotation brings the rolling moment due to aileron, $L_\xi,\,F_\phi\,\phi$, into an opposing phase to the original roll excitation (i.e. mainly opposing $L_\beta\,\beta$), cancelling most of this. Thus the two impedance terms $A\ddot\phi$ and $L_\phi\,\phi$ are much reduced in magnitude, together with the Dutch-roll ratio.

This latter effect is, of course, what pilots naturally expected from this type of automatic aileron control and what in fact they found in practice when told to increase the autopilot gain to such high values. The paradoxical effect of increased Dutch-roll ratio at small gain settings, however, that first puzzled them, may now be understood in the light of what is said above and illustrated in Fig. 26.

Next the drastic improvement in damping of the yaw oscillation may be explained with the aid of the remaining two sets of vector polygons, Figs. 27 and 28. It has been demonstrated (*see* section 4) that an important part of the total Dutch-roll damping may be achieved by means of a phase advance of sideslip against yaw. Its magnitude is indicated by a correspondingly large negative angle $\varepsilon_\psi$ in the triangle of kinematic relations, which is usually combined with the polygon of sideforces (*compare* Fig. 5). Fig. 27 shows these polygons for the different aileron gearing values chosen. The anti-clockwise rotation of the rolling phase with increasing $F_\phi$ observed earlier in Fig. 26 also rotates the vector $W\phi$ (gravity component in $y$-direction) in the diagrams of Fig. 27. Thereby $\varepsilon_\psi$, first positive, turns negative, i.e. the initial phase lag of $\beta$ against $\psi$ is changed into a lead, and this lag or lead is directly added to the apex angle of the corresponding isosceles triangle in the polygons of yawing moments, Fig. 28. The greatest beneficial effect will be noted in the polygon for $F_\phi = 0.4$. Beyond this value the $W\phi$ vector in Fig. 27 is still further rotated in a favourable sense, but the length of this vector decreases proportionately with the rapid reduction of the Dutch-roll ratio. Thus for $F_\phi = 2$ the contribution of this vector to the magnitude of negative $\varepsilon_\psi$ has become negligible despite the fact that its phase is the most favourable possible, *viz.* in line with $Y_\beta\,\beta$.

### 5.3. Gyro Tilt Effect.

An effect that bother designers of yaw autostabilizers is that the yaw-rate gyro used with such equipment is normally fixed to the airframe and its reference system, and therefore, with changing incidence, does not measure rate of yaw as defined in aerodynamic-body axes. At high incidence, for instance, it picks up some of the roll-rate component of the Dutch-roll motion and thereby not only changes the magnitude of its output signal but also its phasing with respect to true $\psi$. Here again the fact that the time-vector method stresses the phase relationship between the parameters of motion suggests that it may also be a most suitable method to investigate this gyro problem. This is indeed the case as will be seen immediately.

In Fig. 29 the rate gyro is shown schematically as it is installed in an aircraft at incidence $\alpha$ and, for generality, with an additional inclination $\varepsilon$ of the gyro frame axis with respect to the fuselage longitudinal axis. The gyro measures any component of an aircraft rotation that lies along its sensitivity axis. If rate of yaw and rate of roll during a Dutch-roll oscillation are considered, the total gyro signal can be expressed as

$$\dot\psi_G = \dot\psi\,\cos\,(\alpha+\varepsilon)+\dot\phi\,\sin\,(\alpha+\varepsilon).$$

19

It must be remembered here that $\psi$ and $\phi$ are not coincident in phase, so that at any particular instant one or the other of the two terms on the right hand side of the equation may dominate.

However, both components may be added vectorially in the phase plane as shown in Fig. 30. In this diagram $\psi$ is assumed to have unit length and is oriented along the positive ordinate axis. The roll rate, $\dot{\phi}$, for the particular incidence or airspeed is shown with a phase lag of about 160°. The resultant total gyro signal according to the above equation is shown to be nearly 90° out of phase with true $\psi$ and much reduced in magnitude.

In Fig. 31a this process has been repeated for the sample aircraft (corresponding to that of 4.2) for different airspeeds but without additional gyro tilt angle, $\varepsilon$. The end points of all $\psi_G$—vectors may be joined together in a locus curve for the whole airspeed range as shown by a dotted line. The gyro reads reasonably well at the high speed end, but produces far too small and lagged signals at low speed.

In Fig. 31b it is demonstrated how additional gyro tilt can, at constant aircraft incidence, radically affect the gyro signal; an improvement is obtained for $\varepsilon$ negative (gyro tilted down) and a deterioration for $\varepsilon$ positive.

In Fig. 31c such gyro tilt has been applied to improve the locus of the gyro signal. The low speed end has become acceptable, and at high speed some additional gain of the gyro signal has been achieved together with some slight phase advance. This is quite welcome in order to compensate for some servo lag of the autostabilizer at the higher Dutch-roll frequency connected with high airspeed. On the other hand the aileron control characteristics of the aircraft have been affected, because any rolling motion besides that occurring during Dutch-roll, e.g. in manoeuvres, now produces some autostabilizer induced rudder deflection. Therefore the method has to be applied judiciously. It has, however, proved to be very effective in some practical cases.

### 6. *Conclusions.*

The time vector method was described in Ref. 1 as a means of analysing oscillation problems, using the short period longitudinal aircraft oscillation and the phugoid motion to explain the application of the method.

The present report extends the time vector method to the perhaps more interesting and varied field of aircraft lateral oscillations. Two procedures are described for constructing the vector diagrams: a graphical method, and, for more frequent use, a system of specially constructed calculators.

Some examples are given in detail to show how the shape of the vector polygons varies with aircraft configuration and flight condition. Some aspects of automatic control are also described.

The present report has been restricted to steady straight and level flight. The method could be extended to climbing and turning flight. More complicated forms of automatic control could also be considered.

Although digital computers are available now to do the basic stability analysis, the time vector method still has a useful role as an aid to a physical understanding of the results.

# LIST OF SYMBOLS

| | |
|---|---|
| $A$ | Moment of inertia in roll |
| $C$ | Moment of inertia in yaw |
| $C_L$ | Lift coefficient |
| $c$ | Spring-stiffness factor |
| $E$ | Product of inertia |
| $e$ | Base of natural logarithms |
| $F_\phi$ | Gearing of automatic control |
| $i_A, i_C, i_E$ | Inertia coefficients |
| $k$ | Damping factor |
| $L_\beta, L_\psi, L_\phi, L_p, L_r, L_\xi$ | Dimensional stability derivatives in roll |
| $l_v, l_r, l_p$ | Non-dimensional stability derivatives (*see* Ref. 23) |
| $M$ | Mach number |
| $m$ | Mass |
| $N_\beta, N_\psi, N_\phi$ | Dimensional stability derivatives in yaw |
| $n_v, n_r, n_p$ | Non-dimensional stability derivatives |
| $P$ | Period ($= 2\pi/\omega$) |
| $p, r$ | Components of angular velocity (roll, yaw) |
| $R_E$ | Roll excitation vector ⎫ |
| $R_I$ | Roll inertia vector ⎬ (*see* Fig. 5) |
| $R_\omega$ | Frequency correction parameters |
| $t$ | Time |
| $\hat{t}$ | Unit of aerodynamic time |
| $t_D$ | Damping time |
| $V_e$ | Equilibrium (true) airspeed |
| $V_i$ | Equivalent airspeed |
| $v$ | Velocity component along $y$-axis |
| $\hat{v}$ | $= v/V_e$ |
| $W$ | Aircraft weight |
| $x$ | Displacement |
| $x_0$ | Initial displacement |
| $x_1$ | Arbitrary initial condition |
| $Y_\beta, Y_\phi, Y_\psi$ | Dimensional stability derivatives, sideforce |
| $y_v, y_p, y_r$ | Non-dimensional stability derivatives |

| | |
|---|---|
| $\alpha$ | Angle of incidence relative to body datum line |
| $\alpha_I$ | Angle of incidence relative to principal inertia axis |
| $\beta$ | Angle of sideslip $(= -\hat{v})$ |
| $\gamma_e$ | Equilibrium climb angle |
| $\Delta$ | Inclination of roll axis to principal axis (*see* Fig. 24) |
| $\delta$ | Logarithmic decrement $(= 2\pi \tan \varepsilon_D)$ |
| $\varepsilon$ | Gyro inclination angle (*see* Fig. 29) |
| $\varepsilon_D$ | Damping angle |
| $\varepsilon_x$ | Phase angle of $x$ relative to some datum |
| $\varepsilon_\phi, \varepsilon_\psi$ | Phase angle of $\phi(\psi)$ relative to $\beta$ |
| $\varepsilon_{\phi\psi}$ | Phase angle of $\phi$ relative to $\psi$ |
| $\eta$ | *See* Fig. 5a |
| $\lambda$ | $= \dfrac{\|l_p\|}{i_A \hat{\omega}_0}$ |
| $\mu_2$ | Relative density parameter $= \dfrac{m}{\rho S \dfrac{b}{2}}$ |
| $\phi$ | Bank-angle perturbation |
| $\chi$ | Track-angle perturbation |
| $\psi$ | Heading-angle perturbation |
| $\psi_G$ | Gyro signal |
| $\Omega$ | Resultant angular velocity (*see* Fig. 24) |
| $\omega$ | Damped frequency |
| $\omega_0$ | Undamped natural frequency |
| $\hat{\omega}_0$ | $= \omega_0 \hat{t}$ |
| $\phi/\beta$ etc. | Amplitude ratio |
| $\cdot$ | Indicates differentiation with respect to time |
| $-$ | Indicates a time-vector |

# REFERENCES

| No. | Author(s) | Title, etc. |
|---|---|---|

1   K. H. Doetsch ..      ..      ..      The time vector method for stability investigations.
A.R.C. R. & M. 2945 (1953).

2   K. Mitchell    ..      ..      ..      A routine for lateral stability calculations.
R.A.E. Technical Note Aero 1344 (A.R.C. 7498) (1943).

3   H. R. Hopkin ..      ..      ..      Routine computing methods for stability or response investigations on linear systems.
A.R.C. R. & M. 2392 (1950).

4   W. O. Breuhaus      ..      ..      Resumé of the time vector method as a means for analysing aircraft stability problems.
WADC TR 52–299, P.45828 (1952).

5   P. Lecomte    ..      ..      ..      *Mécanique du vol, les qualités de vol des avions et des engins.*
Dunod, Paris, pp. 253–260 (1962).

6   L. Sternfield    ..      ..      ..      A vector method approach to the analysis of the dynamic lateral stability of aircraft.
*J. Aero. Sci. 21*, 4, pp. 251–256 (1954).

7   K. H. Doetsch ..      ..      ..      Explanation of poorly damped lateral oscillations during automatic approach with aileron steering.
A.R.C. R. & M. 3159 (1958).

8   K. H. Doetsch ..      ..      ..      Probleme der Automatischen Steuerung von Flugzeugen, *Jahrbuch der WGL*, pp. 72–78 (1955).

9   K. H. Doetsch ..      ..      ..      Selected problems of dynamic stability.
R.A.E. Trans. 803, 1959, also *WGL Jahrbuch* 1954, pp. 95–103.

10   C. L. Gillis, J. L. Mitchell and C. T. D'Aiutolo      Determination of lateral stability characteristics from free-flight model tests, with experimental results on the effects of wing vertical position and dihedral at transonic speeds.
NASA TR R–65 (1960).

11   E. E. Larrabee ..      ..      ..      Application of the time vector method to the analysis of flight test lateral oscillation data.
FRM 189 Cornell Aero. Lab. Inc. (1953).

12   H. C. Lyster    ..      ..      ..      A critical review of techniques for the flight determination of aircraft dynamic stability and response characteristics with illustrative examples from measurements on a subsonic jet fighter.
NRC Report LR–336, P.106230 (1962).

23

REFERENCES—*continued*

| No. | Author(s) | Title, etc. |
|---|---|---|

13  R. Rose .. .. .. .. Flight measurements of the Dutch-roll characteristics of a 60 degree delta wing aircraft (Fairey Delta 2) at Mach numbers from 0·4 to 1·5 with stability derivatives extracted by vector analysis.
A.R.C. C.P. 653 (1961).

14  K. J. Turner .. .. .. Measurements of dynamic stability from three simplified free-flight models of a supersonic research aircraft (Bristol ER.134) over the Mach number range 1·2–2·6.
A.R.C. C.P. 816 (1961).
AGARD Report 378 (1961).

15  C. H. Wolowicz .. .. Time-vector determined lateral derivatives of a swept-wing fighter-type airplane with three different vertical tails at Mach numbers between 0·7 and 1·48.
NACA RM H 56C20, TIL 6508 (1956).

16  C. H. Wolowicz and .. .. Stability derivative determination from flight data. Presented to
E. C. Holleman Flight Test Panel, AGARD, Copenhagen.
AGARD Rep. 224 (A.R.C. 20583) (1958).

17  C. H. Wolowicz and .. .. Stability derivative determination from flight data.
E. C. Holleman AGARD Flight test Manual, Vol. II, Chapter 10, part II, p. 10:35.

18  W. H. Andrews and .. .. Flight determined stability and control derivatives of a supersonic
H. A. Rediess airplane with a low-aspect ratio unswept wing and a tee-tail.
NASA Memo 2–2–59 H, TIL 6776 (1959).

19  J. E. Nethaway and J. Clark .. Flight tests to investigate the dynamic lateral stability characteristics of a 45 deg. delta, cropped to give three aspect ratios.
A.R.C. R. & M. 3243 (1960).

20  D. H. Perry, J. C. Morrall .. Low speed flight tests on a tailless delta aircraft with wings swept
and W. G. A. Port back 44·5° (Avro 707 B). Part 3. Lateral stability and control.
R.A.E. Report Aero 2638 (A.R.C. 22242) (1960).

21  D. H. Perry .. .. .. Flight tests of the lateral stability of the De Havilland Sea Venom with blowing over the flaps.
R.A.E. Technical Note Aero 2668 (A.R.C. 22055) (1960).

22  H. R. Hopkin .. .. .. A scheme of notation and nomenclature for aircraft dynamics and associated aerodynamics.
R.A.E. Technical Report 66200 (1966). A.R.C. 28969. To be published as A.R.C. R. & M. 3562, Part 1.

23  L. W. Bryant and S. B. Gates.. Nomenclature for stability coefficients.
A.R.C. R. & M. 1801 (1937).

REFERENCES—*continued*

| *No.* | *Author(s)* | *Title, etc.* |
|---|---|---|

24  H. H. B. M. Thomas and    ..  Interim note on stability and response characteristics of super-
S. Neumark                         sonic aircraft (linear theory).
R.A.E. Technical Note Aero 2412 (1955). A.R.C. 18263.

25  A. J. Ross    ..    ..    ..  The lateral oscillation of slender aircraft.
A.R.C. C.P. 845 (1962).

TABLE 1

*Graphical Solution.*

*Dutch-Roll Oscillation.*

| AIRCRAFT | | | | Cmptd. by | Date |
|---|---|---|---|---|---|
| Altitude | ft | $C_L$ | $M$ | | |
| $\mu_2$ | $\hat{t}$ | $i_A$ | $i_C$ | | |
| Initial Approx.: $\hat{\omega}_0^2 = \mu_2\, n_v/i_C + \mu_2\, l_V/i_A \cdot i_E/i_C\,;\, \psi/\beta = 1\,;\, \varepsilon_D = 0\,;\, \varepsilon_\psi = 0$ | | | | | |

| ROLLING MOMENTS | | | $\hat{\omega}_0^2$ | | | | | Phase |
|---|---|---|---|---|---|---|---|---|
| | | | $\hat{\omega}_0$ | | | | | |
| $l_v$ | $\mu_2\, l_v/i_A$ | | | | | | | |
| $l_r$ | $l_r/\mu_2\, l_v$ | $\times\ \hat{\omega}_0\, \psi/\beta$ | | | | | | $+\dot{\psi}$ |
| $i_E$ | $i_E/\mu_2\, l_v$ | $\times\ \hat{\omega}_0^2\, \psi/\beta$ | | | | | | $\mp\ddot{\psi}$ |
| $l_p$ | $l_p/i_A$ | $\div\ \hat{\omega}_0$ | ⓛ | | | | | $-\dot{\phi}$ |
| $\eta = \tan^{-1}\left[ⓛ\cos \varepsilon_D/1 - ⓛ\sin \varepsilon_D)\right]$ | | | | | | | | |
| From Diagram | Roll Inertia $\qquad R_I$ | | | | | | | |
| Roll-Sideslip Ratio $\phi/\beta = \mu_2\, l_v/i_A \times R_I/\hat{\omega}_0^2$ | | | | | | | | |

| Y-FORCES | | | | | | | | |
|---|---|---|---|---|---|---|---|---|
| $y_v$ | | $\div\ \hat{\omega}_0$ | | | | | | $+\bar{\beta}$ |
| $\frac{1}{2} C_L$ | | $\times\ 1/\hat{\omega}_0\, \phi/\beta$ | | | | | | $+\bar{\phi}$ |
| $y_p$ | $y_p/\mu_2$ | $\times\ \phi/\beta$ | | | | | | $-\dot{\phi}$ |
| From diagram | Yaw Ratio $\qquad \psi/\beta$ | | | | | | | |
| | Yaw Phase $\qquad \varepsilon_\psi$ | | | | | | | |
| Dutch Roll Ratio $\phi/\psi = \phi/\beta \div \psi/\beta$ | | | | | | | | |

TABLE 1—*continued*

| YAWING MOMENTS | | | | | | | | |
|---|---|---|---|---|---|---|---|---|
| $n_v$ | $\mu_2\, n_v/i_C$ | $\div\, \hat{\omega}_0^2\, \psi/\beta$ | | | | | | $-\bar{\beta}$ |
| $i_E$ | $i_E/i_C$ | $\times\, \phi/\psi$ | | | | | | $\mp\ddot{\bar{\phi}}$ |
| $n_p$ | $n_p/i_C$ | $\times\, 1/\hat{\omega}_0\, \phi/\psi$ | | | | | | $\mp\dot{\bar{\phi}}$ |
| $n_r$ | $n_r/i_C$ | $\div\, \hat{\omega}_0$ | | | | | | $-\dot{\bar{\psi}}$ |
| From diagram | Damping Angle $\varepsilon_D$ | | | | | | | |
| | Frequency Correction $R_\omega$ | | | | | | | |
| New $\hat{\omega}_0^2$ = previous $\hat{\omega}_0^2 \times R_\omega$ | | | | | | | | |

| RESULTS | $\hat{\omega}_0$ | $\varepsilon_D$ | $P$ | $p/r$ | $\delta$ |
|---|---|---|---|---|---|
| | | | | | |

TABLE 2

*Graphical Solution—Worked Example.*

*Dutch-Roll Oscillation.*

| AIRCRAFT | | | | Cmptd. by | Date |
|---|---|---|---|---|---|
| Altitude 5000 ft | $C_L$ 0·6 | | $M$ 0·33 | | |
| $\mu_2$ 31·2 | $\hat{t}$ 3·45 | $i_A$ 0·064 | $i_C$ 0·166 | | |
| Initial Approx.: $\hat{\omega}_0^2 = \mu_2\, n_v/i_C + \mu_2\, l_V/i_A \cdot i_E/i_C$; $\quad \psi/\beta = 1$; $\varepsilon_D = 0$; $\varepsilon_\psi = 0$ | | | | | |

| ROLLING MOMENTS | | | $\hat{\omega}_0^2$ | 32·5 | 39·4 | 38·6 | | Phase |
|---|---|---|---|---|---|---|---|---|
| | | | $\hat{\omega}_0$ | 5·70 | 6·27 | 6·21 | | |
| $l_v - 0·115$ | $\mu_2\, l_v/i_A$ | 56 | | | | | | |
| $l_r + 0·130$ | $l_r/\mu_2\, l_v$ | 0·0362 | $\times\ \hat{\omega}_0\ \psi/\beta$ | 0·206 | 0·212 | 0·217 | | $+\ddot{\psi}$ |
| $i_E - 0·038$ | $i_E/\mu_2\, l_v$ | 0·0106 | $\times\ \hat{\omega}_0^2\ \psi/\beta$ | 0·345 | 0·388 | 0·395 | | $\mp\ddot{\psi}$ |
| $l_p - 0·225$ | $l_p/i_A$ | 3·52 | $\div\ \hat{\omega}_0$ | (λ) 0·618 | 0·561 | 0·566 | | $-\dot{\phi}$ |
| $\eta = \tan^{-1}\left[(\lambda)\cos \varepsilon_D/(1 - (\ )\sin \varepsilon_D)\right]$ | | | | 32·8° | 30·8° | 31·6° | | |
| From Diagram | Roll Inertia | $R_I$ | | 1·15 | 1·28 | 1·29 | | |
| Roll-Sideslip Ratio $\phi/\beta = \mu_2\, l_v/i_A \times R_I/\hat{\omega}_0^2$ | | | | 1·98 | 1·82 | 1·87 | | |

| Y-FORCES | | | | | | | | |
|---|---|---|---|---|---|---|---|---|
| $y_v - 0·250$ | | | $\div\ \hat{\omega}_0$ | 0·0438 | 0·0398 | 0·0402 | | $+\bar{\beta}$ |
| $\frac{1}{2} C_L\ 0·3$ | | | $\times\ 1/\hat{\omega}_0\ \phi/\beta$ | 0·104 | 0·087 | 0·0904 | | $+\bar{\phi}$ |
| $y_p$ | $y_p/\mu_2$ | | $\times\ \phi/\beta$ | – | – | – | | $-\dot{\phi}$ |
| From Diagram | Yaw Ratio | $\psi/\beta$ | | 0·93 | 0·965 | 0·965 | | |
| | Yaw Phase | $\varepsilon_\psi$ | | $+2°$ | $+2°$ | $+2·8°$ | | |
| Dutch Roll Ratio $\phi/\psi = \phi/\beta \div \psi/\beta$ | | | | 2·06 | 1·89 | 1·94 | | |

TABLE 2—*continued*

| YAWING MOMENTS | | | | | | | |
|---|---|---|---|---|---|---|---|
| $n_v$ 0·110 | $\mu_2\, n_v/i_C$ 20·7 | $\div\, \hat{\omega}_0^2\, \psi/\beta$ | 0·686 | 0·545 | 0·556 | | $-\bar{\beta}$ |
| $i_E - 0·038$ | $i_E/i_C$ 0·229 | $\times\, \phi/\psi$ | 0·472 | 0·433 | 0·445 | | $\mp\ddot{\phi}$ |
| $n_p - 0·083$ | $n_p/i_C$ 0·50 | $\times\, 1/\hat{\omega}_0\, \phi/\psi$ | 0·181 | 0·151 | 0·156 | | $\mp\dot{\phi}$ |
| $n_r - 0·166$ | $n_r/i_C$ 1·0 | $\div\, \hat{\omega}_0$ | 0·175 | 0·159 | 0·161 | | $-\dot{\psi}$ |
| From Diagram | Damping Angle $\varepsilon_D$ | | 7·5° | 9° | 9° | | |
| | Frequency Correction $R_\omega$ | | 1·21 | 0·98 | 0·993 $\simeq$ 1 | | |
| New $\hat{\omega}_0^2$ = previous $\hat{\omega}_0^2 \times R_\omega$ | | | 39·4 | 38·6 | 38·4 | | |

| RESULTS | $\hat{\omega}_0$ | 6·2 | $\varepsilon_D$ | 9° | $P$ | 3·5 sec | $p/r$ | 1·94 | $\delta$ | 0·995 |
|---|---|---|---|---|---|---|---|---|---|---|

TABLE 3.

*Vector Calculator Solution.*

*Dutch-Roll Oscillation.*

| AIRCRAFT | | | | Cmptd. by | Date |
|---|---|---|---|---|---|
| Altitude ft | | $C_L$ | $M$ | | |
| $\mu_2$ | $\hat{t}$ | $i_A$ | $i_C$ | | |
| Initial Approx.: $\hat{\omega}_0^2 = \mu_2\, n_v/i_C + \mu_2\, l_v/i_A \cdot i_E/i_C$; $\quad \psi/\beta = 1$; $\varepsilon_D = 0$; $\varepsilon_\psi = 0$ | | | | | |

| ROLLING MOMENTS | | | $\hat{\omega}_0^2$ | | | | |
|---|---|---|---|---|---|---|---|
| | | | $\hat{\omega}_0$ | | | | |
| $l_v$ | $\mu_2\, l_v/i_A$ | | | | | | |
| $l_r$ | $l_r/\mu_2\, l_v$ | $\times\ \hat{\omega}_0\, \psi/\beta$ | | | | | |
| $i_E$ | $i_E/\mu_2\, l_v$ | $\times\ \hat{\omega}_0^2\, \psi/\beta$ | | | | | |
| $l_p$ | $l_p/i_A$ | $\div\ \hat{\omega}_0$ | | | | | |
| From Calculator | Resultant Roll Excitation $R_E$ | | | | | | |
| | Roll Inertia $\quad R_I'$ | | | | | | |
| | Roll Acceleration Phase $\quad \varepsilon_{\ddot{\phi}}$ | | | | | | |
| Roll Phase $= \varepsilon_\phi = -(180 + 2\varepsilon_D) + \varepsilon_{\ddot{\phi}}$ | | | | | | | |
| Roll-Sideslip Ratio $\phi/\beta = \mu_2\, l_v/i_A \times R_I'\, R_E/\hat{\omega}_0^2$ | | | | | | | |

| Y-FORCES | | | | | | | |
|---|---|---|---|---|---|---|---|
| $y_v$ | | $\div\ \hat{\omega}_0$ | | | | | |
| $\frac{1}{2} C_L$ | | $\times\ 1/\hat{\omega}_0\ \phi/\beta$ | | | | | |
| $y_p$ | $y_p/\mu_2$ | $\times\ \phi/\beta$ | | | | | |
| From Calculator | Yaw Ratio $\quad \psi/\beta$ | | | | | | |
| | Yaw Phase $\quad \varepsilon_\psi$ | | | | | | |
| Dutch-Roll Ratio $\phi/\psi = \phi/\beta \div \psi/\beta$ | | | | | | | |

TABLE 3—*continued*

| YAWING MOMENTS | | | | | | | |
|---|---|---|---|---|---|---|---|
| $n_v$ | $\mu_2\, n_v/i_C$ | $\div\ \hat{\omega}_0^2\ \psi/\beta$ | | | | | |
| $i_E$ | $i_E/i_C$ | $\times\ \phi/\psi$ | | | | | |
| $n_p$ | $n_p/i_C$ | $\times\ 1/\hat{\omega}_0\ \phi/\psi$ | | | | | |
| $n_r$ | $n_r/i_C$ | $\div\ \hat{\omega}_0$ | | | | | |
| From Calculator | Damping Angle $\qquad \varepsilon_D$ | | | | | | |
| | Frequency Correction $\qquad R_\omega$ | | | | | | |
| New $\hat{\omega}_0^2$ = previous $\hat{\omega}_0^2 \times R_\omega$ | | | | | | | |

| RESULTS | $\hat{\omega}_0$ | $\varepsilon_D$ | $P$ | $p/r$ | $\delta$ |
|---|---|---|---|---|---|
| | | | | | |

$x_o$

$x_o \sec \varepsilon_D$

$t_D$

ENVELOPE $x = |\bar{x}_o| \, e^{-t/t_D}$

t

R

$\varepsilon_D$

$\omega$

$\varepsilon_D$

$\bar{x}_o$

I

(b) TIME HISTORY OF DISPLACEMENT

(c) GENERATING MOTION
OF TIME VECTOR IN
THE PHASE PLANE

(a) PHYSICAL SYSTEM
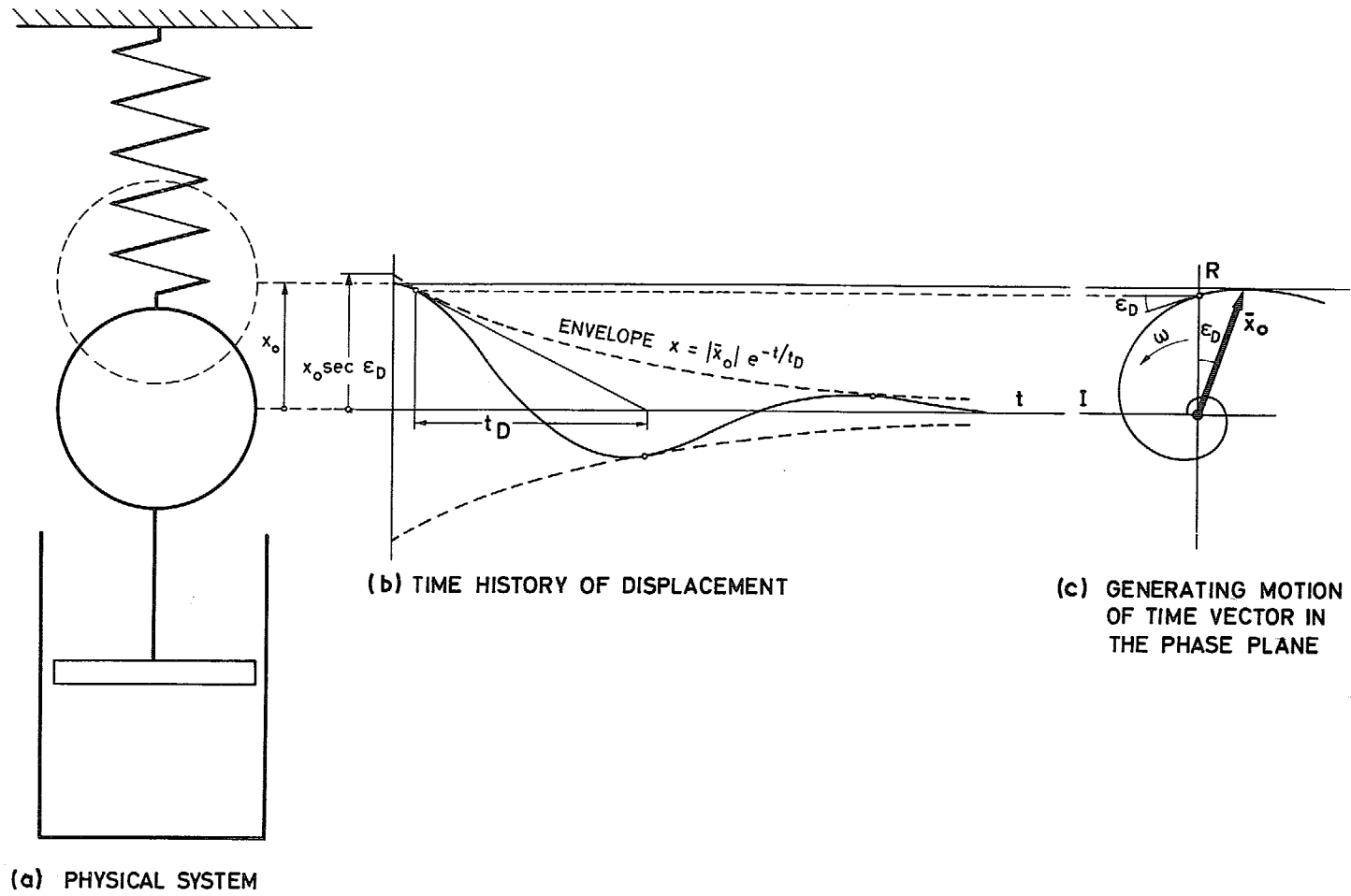
FIG. 1 a to c.   Simple oscillator.

(a) GENERATING TIME VECTORS
    IN THE PHASE PLANE

(b) TIME HISTORIES

(c) TIME VECTORS IN THE PHASE PLANE

(d) POLYGON OF FORCES
    = ISOSCELES TRIANGLE
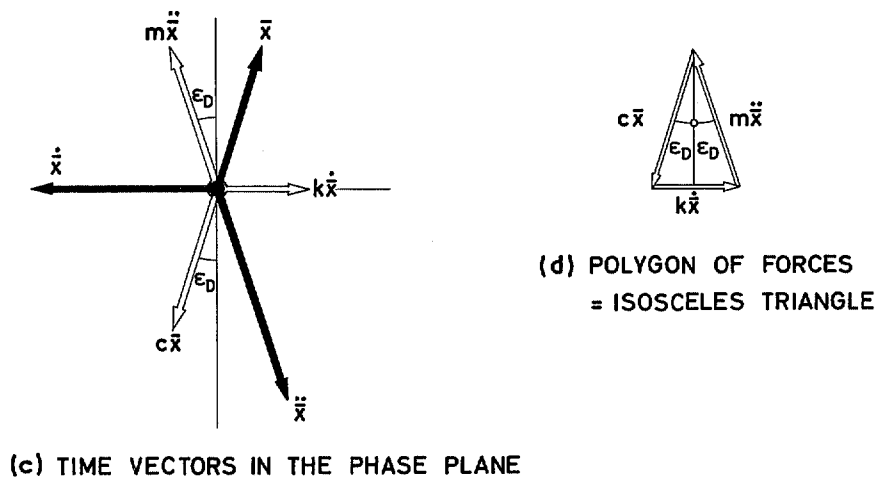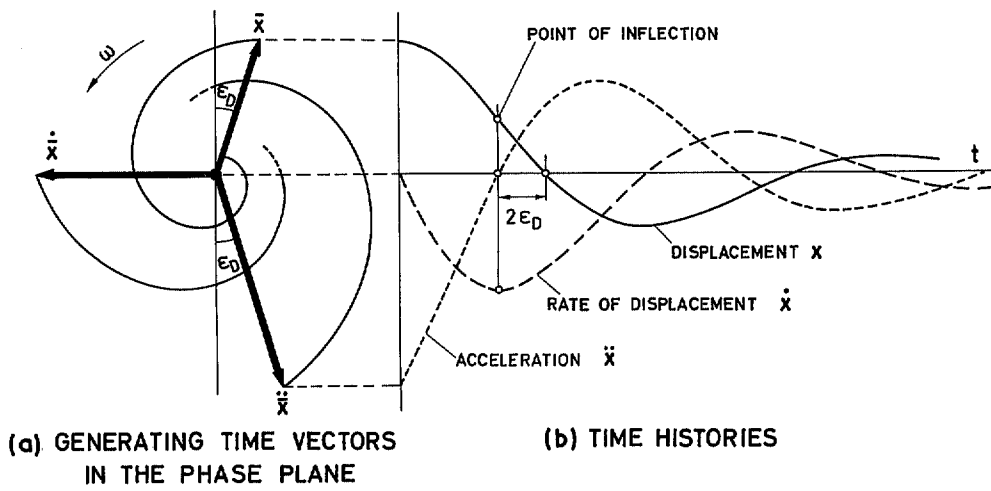
FIG. 2 a to d.   Vector diagram for simple oscillator.



DISTURBED FLIGHT PATH

EQUILIBRIUM FLIGHT PATH

IN LEVEL FLIGHT

$\psi = \chi + \beta$
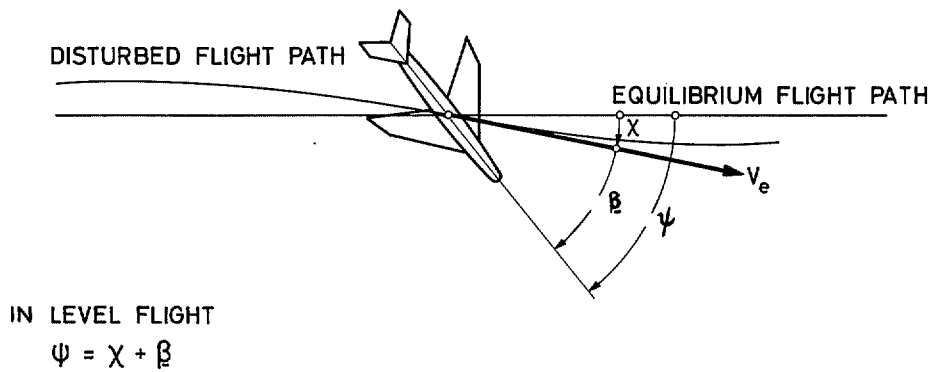
FIG. 3.   Definition of angles.

33

(b) SIDEFORCES

$mV_e\dot{X}$
$Y_\beta\beta$
$W\phi$

$\dot\psi$
$\dot\beta$
$\varepsilon_\psi$

(a) ROLLING MOMENTS

$L_{\dot\phi}\dot\phi$

$A\ddot\phi$

$R_E$

$E\ddot\psi$

$L_{\dot\psi}\dot\psi$

$L_\beta\beta$

$\varepsilon_D = \varepsilon_\psi = 0$

$\dot\psi$

$\beta, \psi$

(c) KINEMATIC RELATION

$X$ $\psi$

$\beta$

$\phi$

(d) YAWING MOMENTS

$N_\beta\beta$

$E\ddot\phi$

$\varepsilon_\psi$ $2\varepsilon_D$

$N_{\dot\phi}\dot\phi$

$N_{\dot\psi}\dot\psi$

$C\ddot\psi$
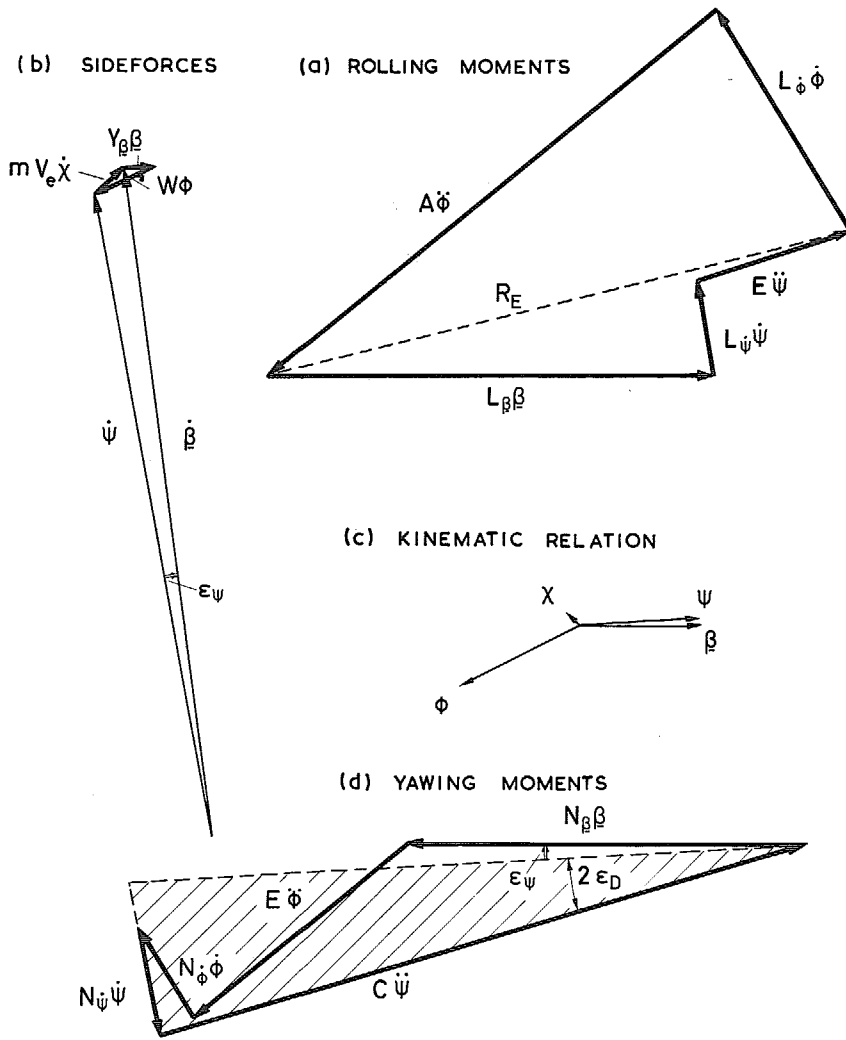
FIG. 4 a to d.  Typical example of vector diagrams.

$\dfrac{y_v}{\hat\omega_o}$

$\dfrac{X}{\beta}$

$\dfrac{C_L}{2\hat\omega_o}\dfrac{\phi}{\beta}$

$\beta$

$\dot X$

$D$

$\dfrac{X}{\beta}$ $F$

$I$

$\dfrac{\psi}{\beta}$

$\varepsilon_\psi$

$E$

$R_I = \dfrac{i_A}{\mu_2 \ell_v}\hat\omega_o^2\dfrac{\phi}{\beta}$

$C$

$\dfrac{i_A}{\mu_2 \ell_v}\hat\omega_o\dfrac{\phi}{\beta}$

$\dfrac{i_E}{\mu_2 \ell_v}\hat\omega_o^2\dfrac{\psi}{\beta}$

$B$

$\eta$

$R_E$

$A$

$I$

$\dfrac{\ell_r}{\mu_2 \ell_v}\hat\omega_o\dfrac{\psi}{\beta}$

(a) ROLLING MOMENT DIAGRAM

$\dfrac{y_v}{\hat\omega_o}$

$D$

$\dfrac{C_L}{2\hat\omega_o}\dfrac{\phi}{\beta}$

$F$

$I$

$\dfrac{\psi}{\beta}$

$\varepsilon_\psi$

$E$

(b) SIDEFORCE AND KINEMATIC DIAGRAMS
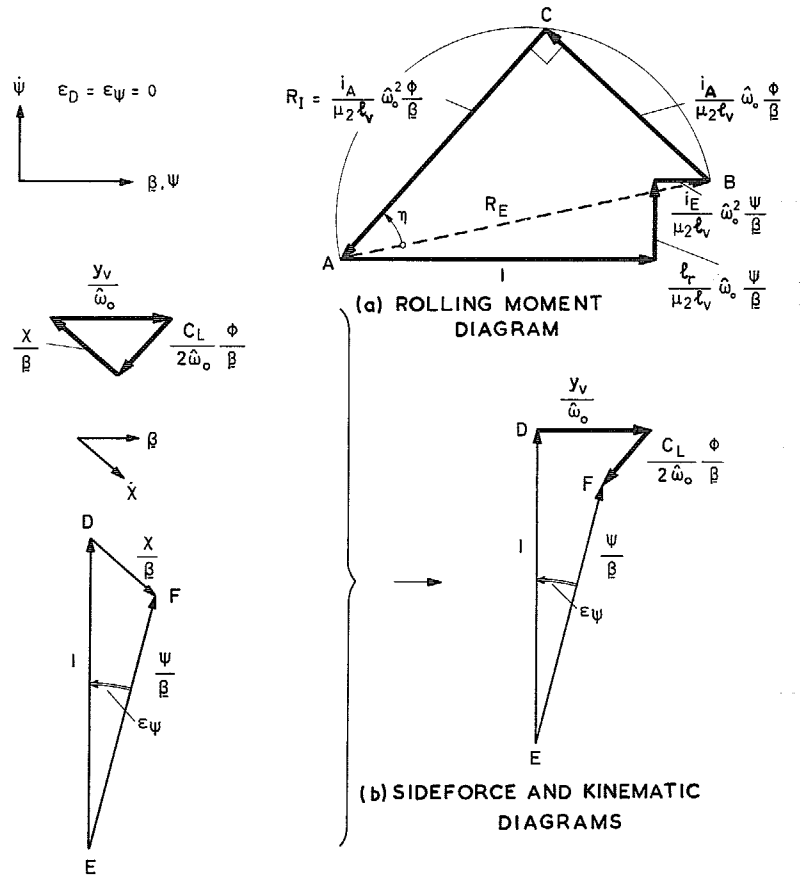
FIG. 5 a & b.  Construction of vector diagrams.

**(c) YAWING MOMENT DIAGRAM**
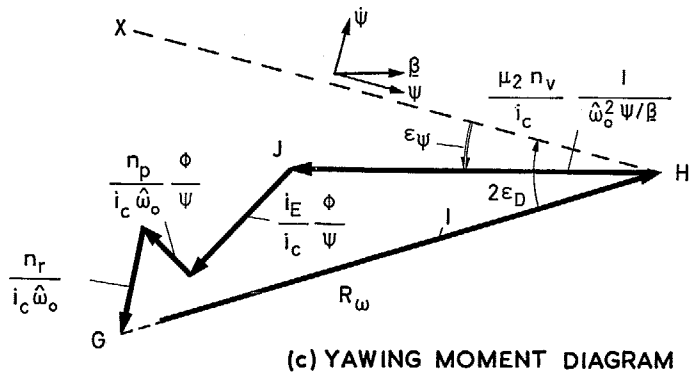
FIG. 5c.   Construction of vector diagrams.
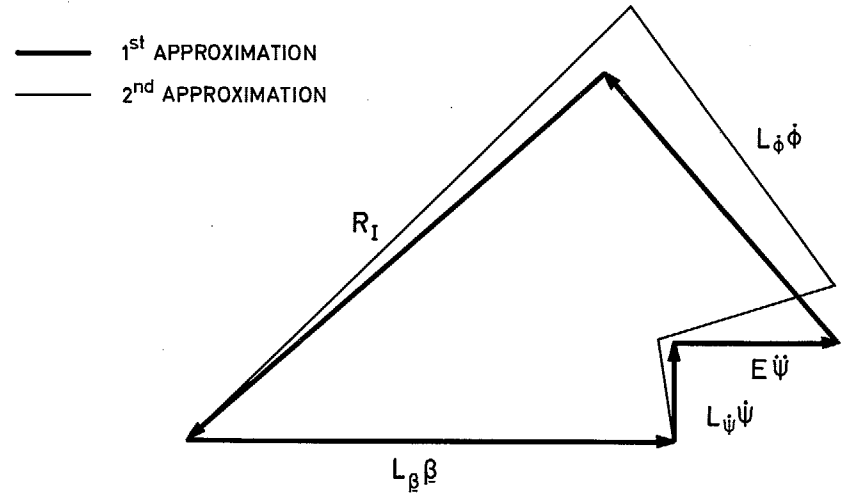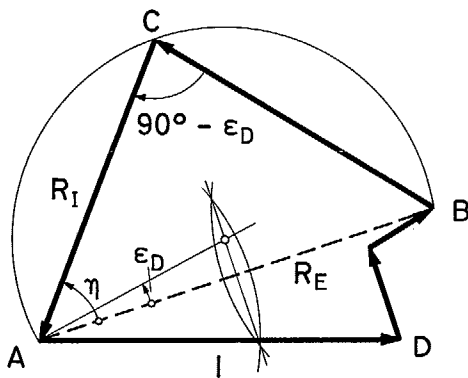
FIG. 6.   Rolling moment diagram. Procedure for
non-zero damping.

1st APPROXIMATION

2nd APPROXIMATION

SEE TABLE 2 FOR DETAILS
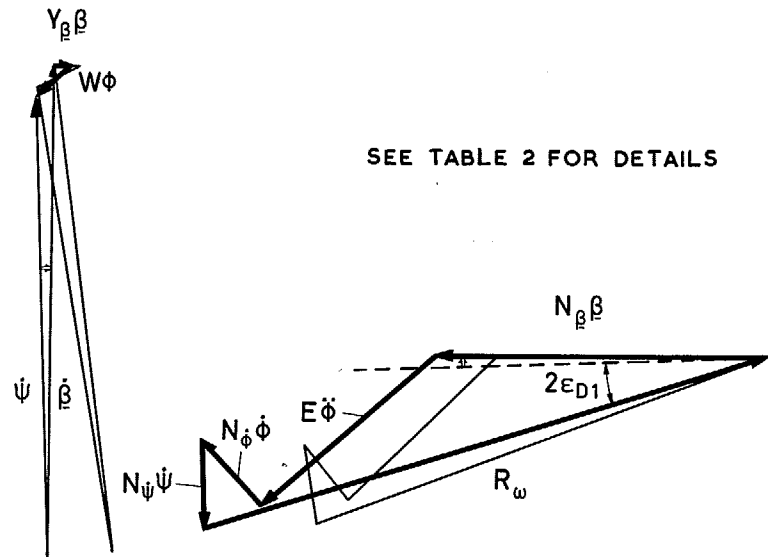
FIG. 7.   Worked example, graphical method, first
and second approximation.
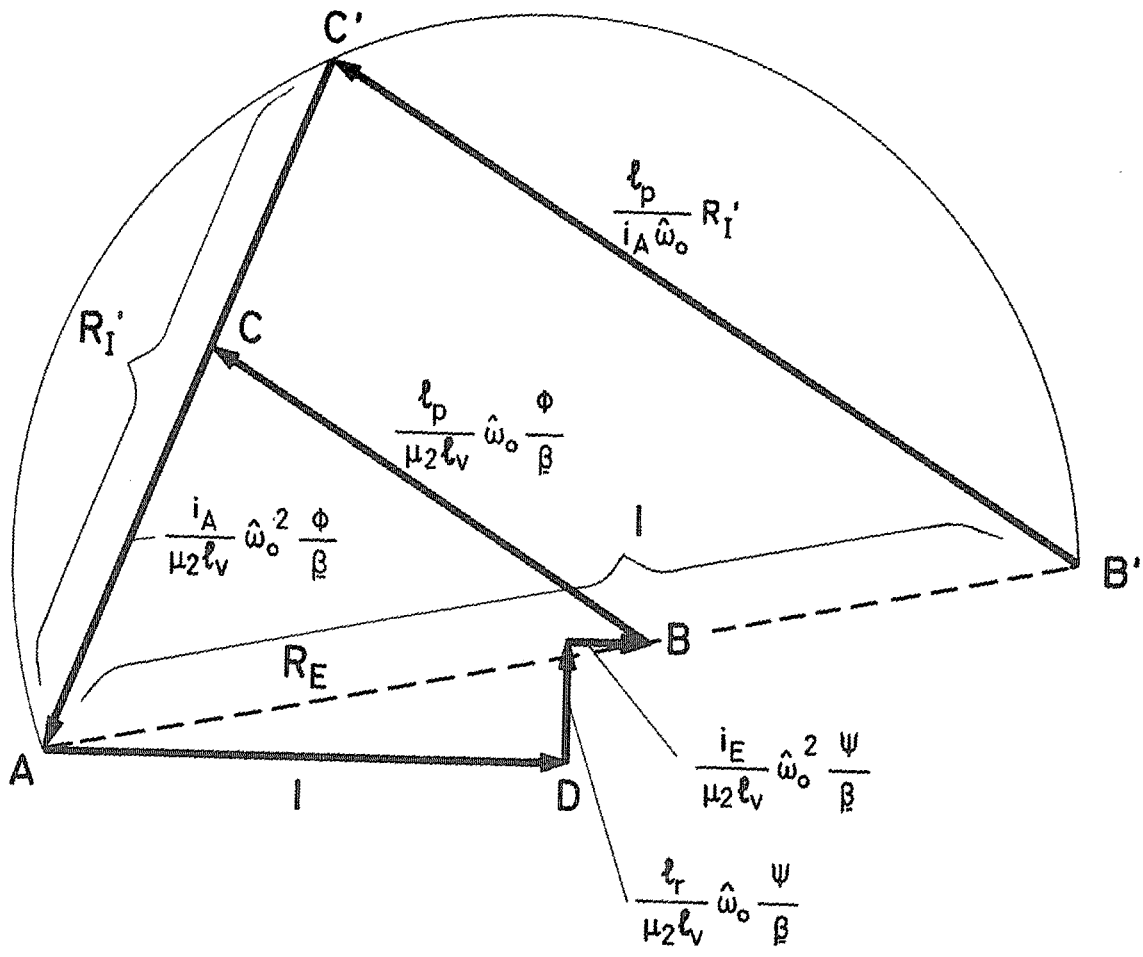
FIG. 8. Mechanization of rolling-moment diagram.
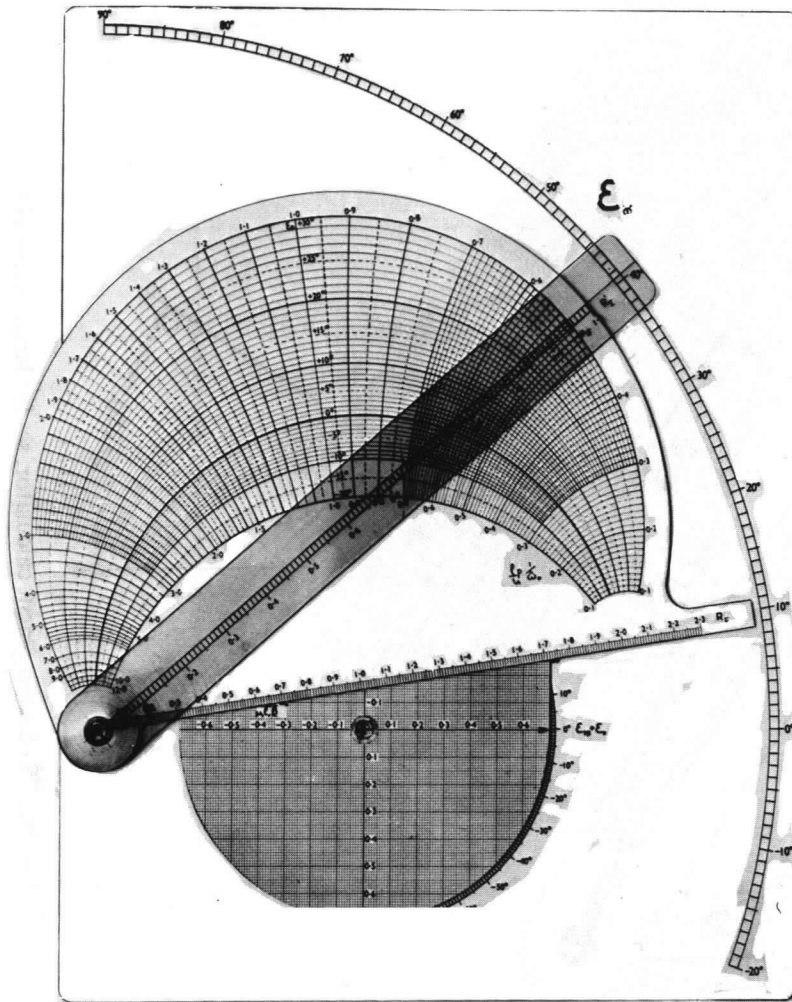
FIG. 9a. Rolling-moment calculator.
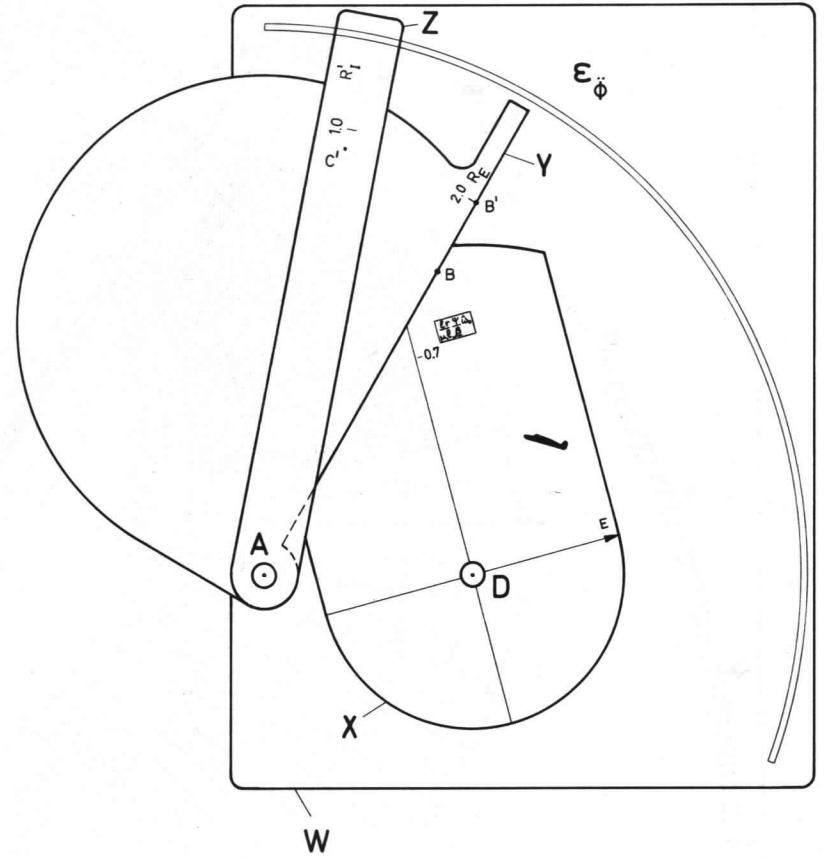


FIG. 9b. Rolling-moment calculator.
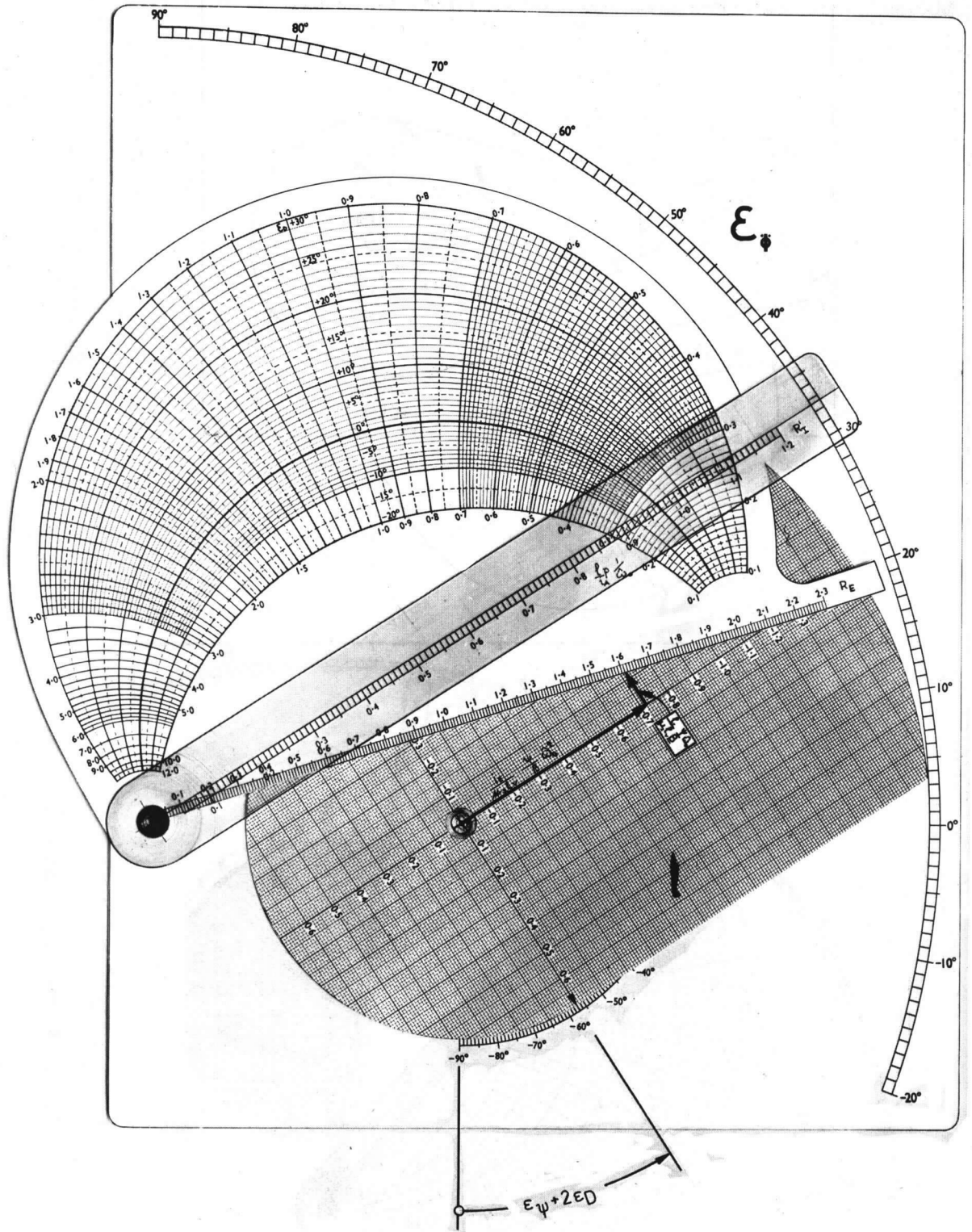
Fig. 9c. Rolling-moment calculator, set for large values of $i_E$.
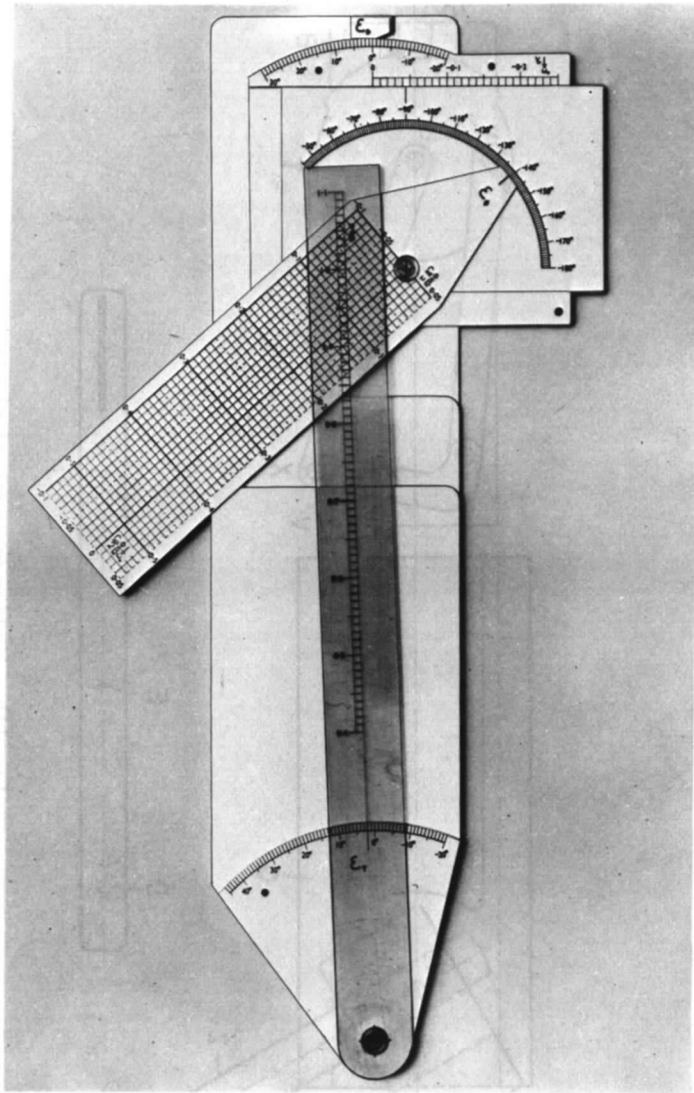
FIG. 10a.   Sideforce calculator.
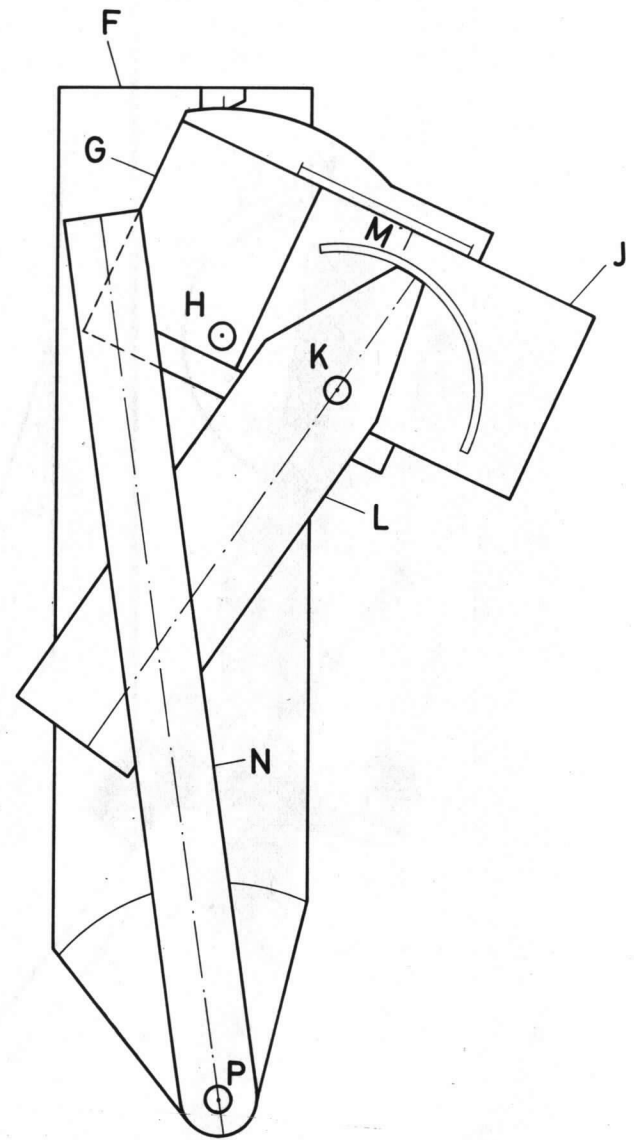
FIG. 10b.   Sideforce calculator.
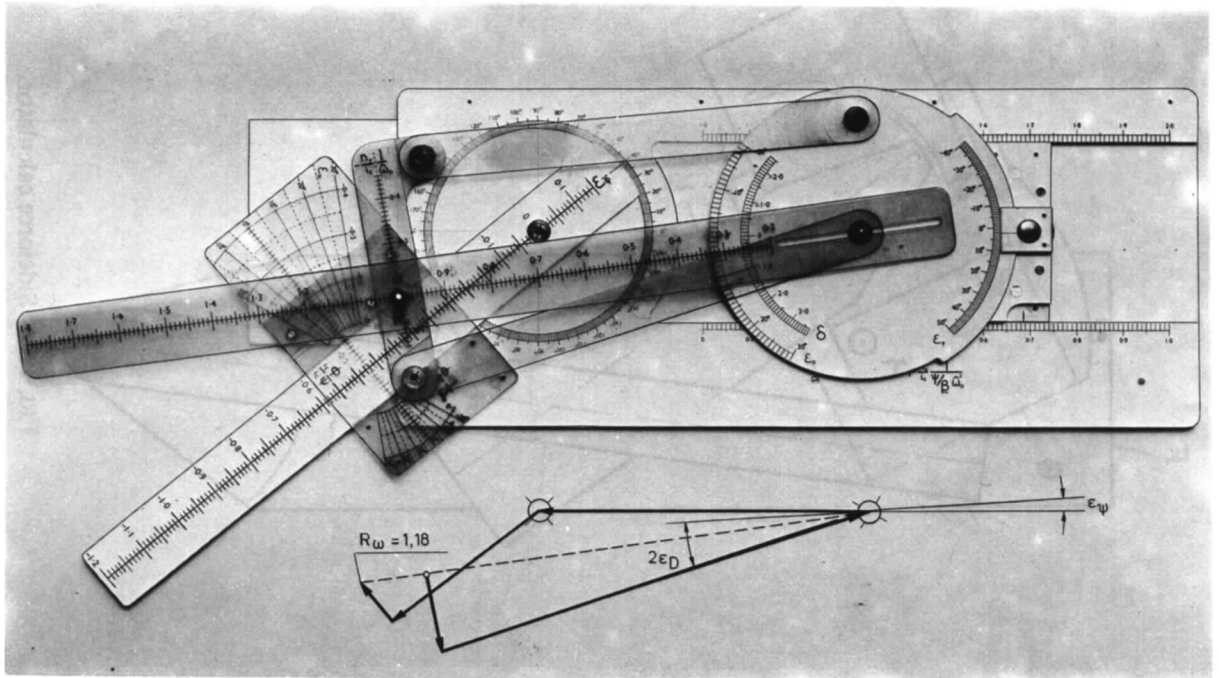
FIG. 11a.  Yawing moment calculator.
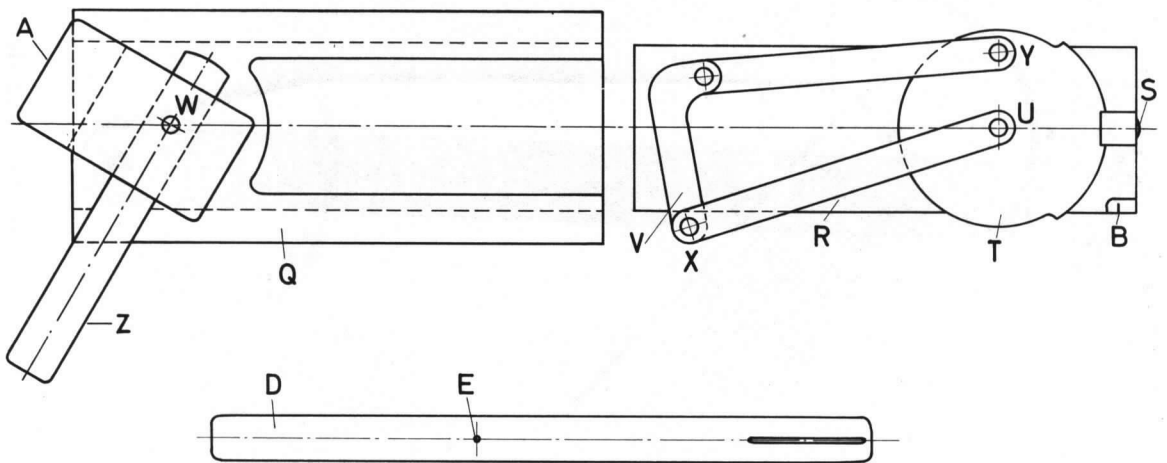


FIG. 11b.  Yawing-moment calculator.

40
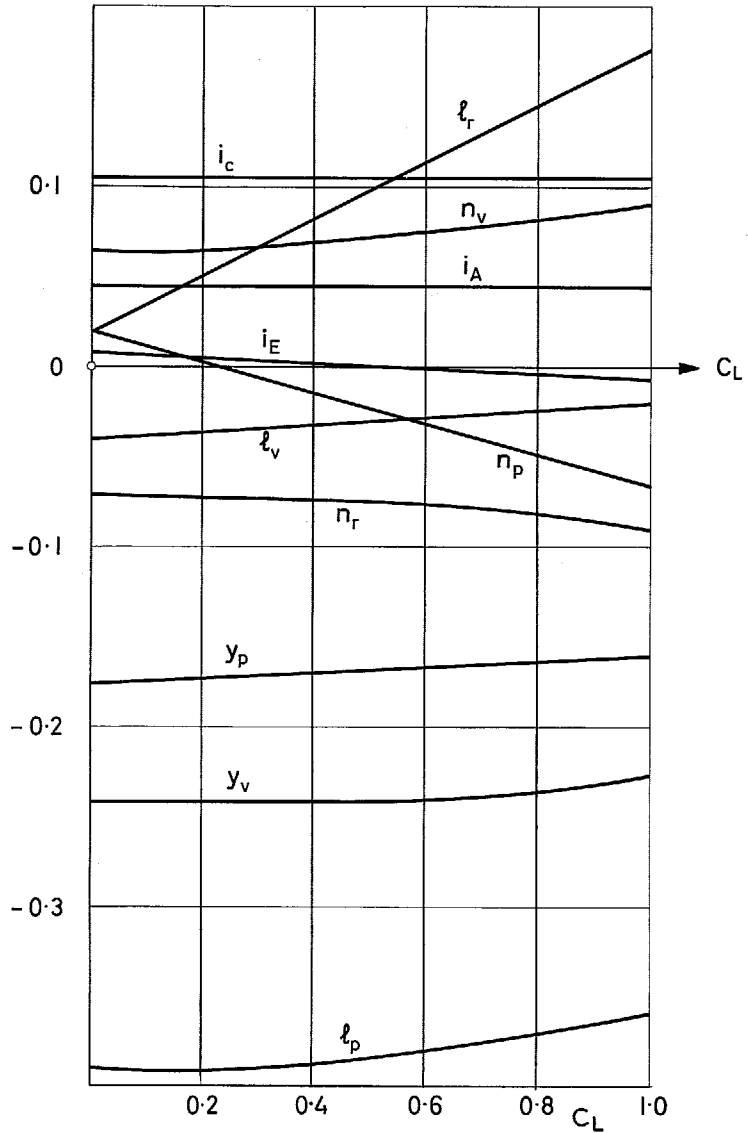
FIG. 12.  High aspect ratio straight-wing aircraft,
lateral derivatives.
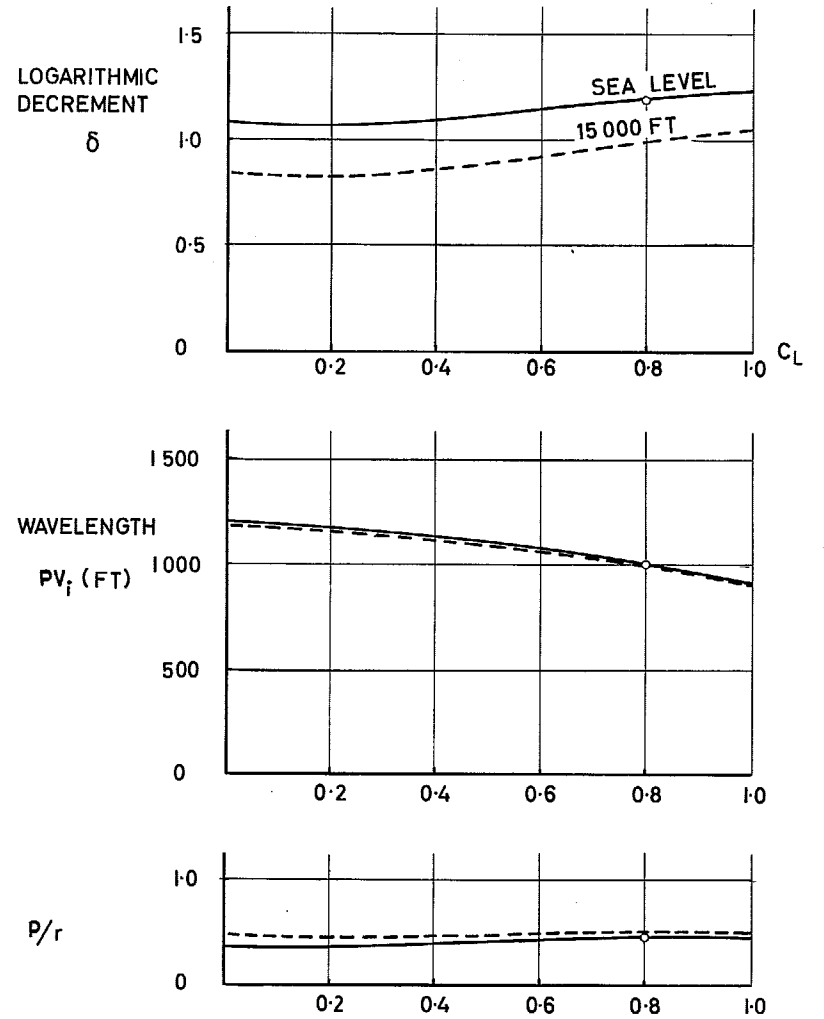


FIG. 13.  High aspect ratio, straight-wing air-
craft, lateral stability characteristics.
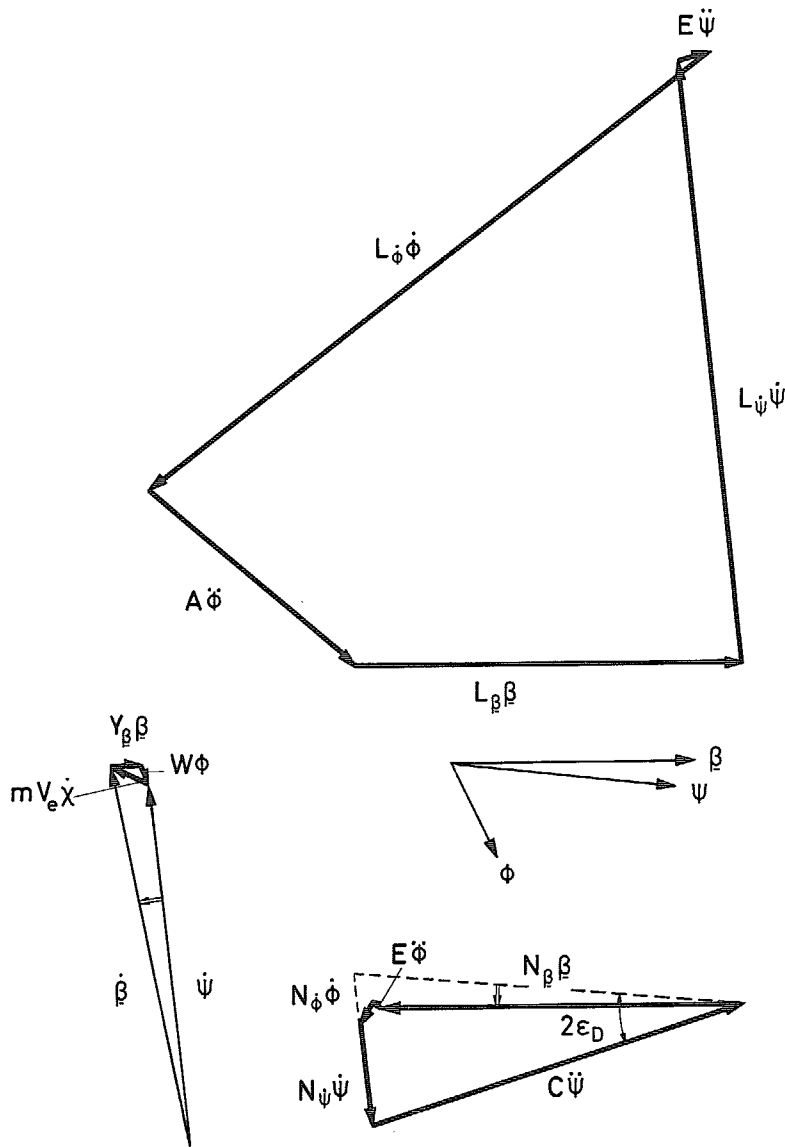
FIG. 14. High aspect ratio, straight-wing aircraft, vector diagrams, $C_L = 0.8$, sea level.
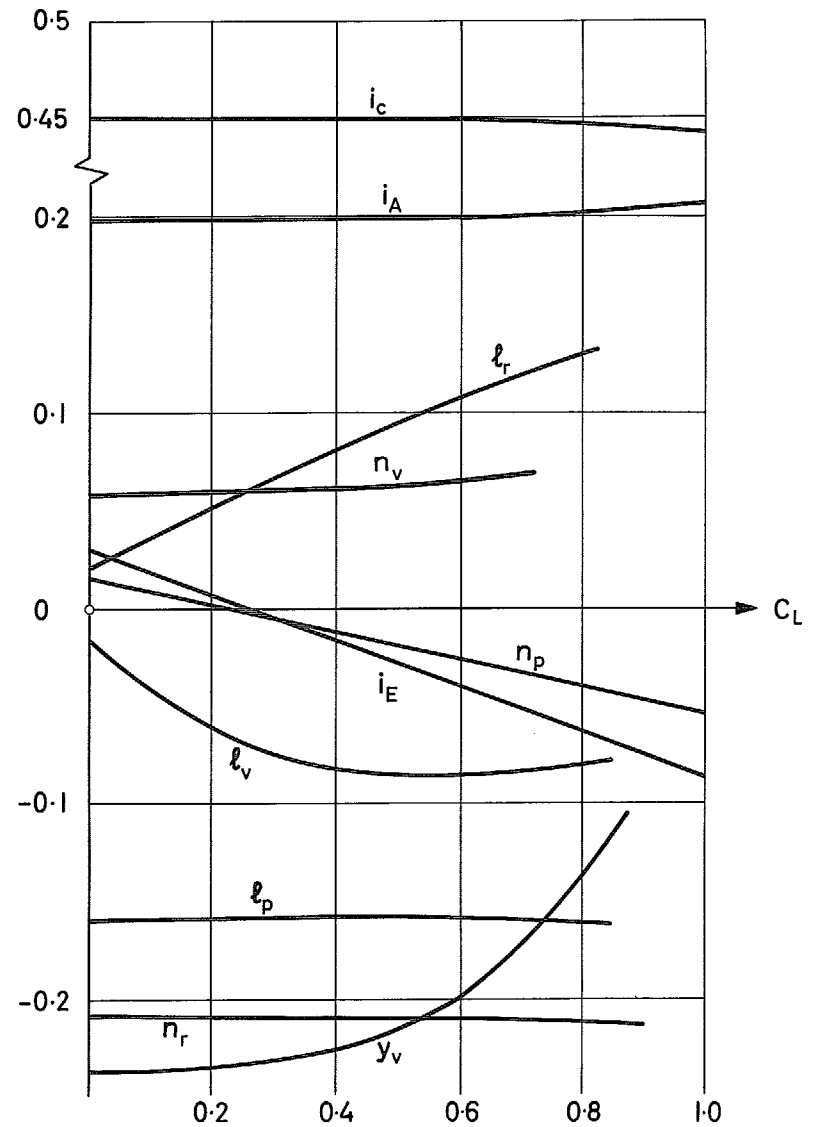
FIG. 15. Delta-wing aircraft $(A.R. = 1.8)$, lateral derivatives.
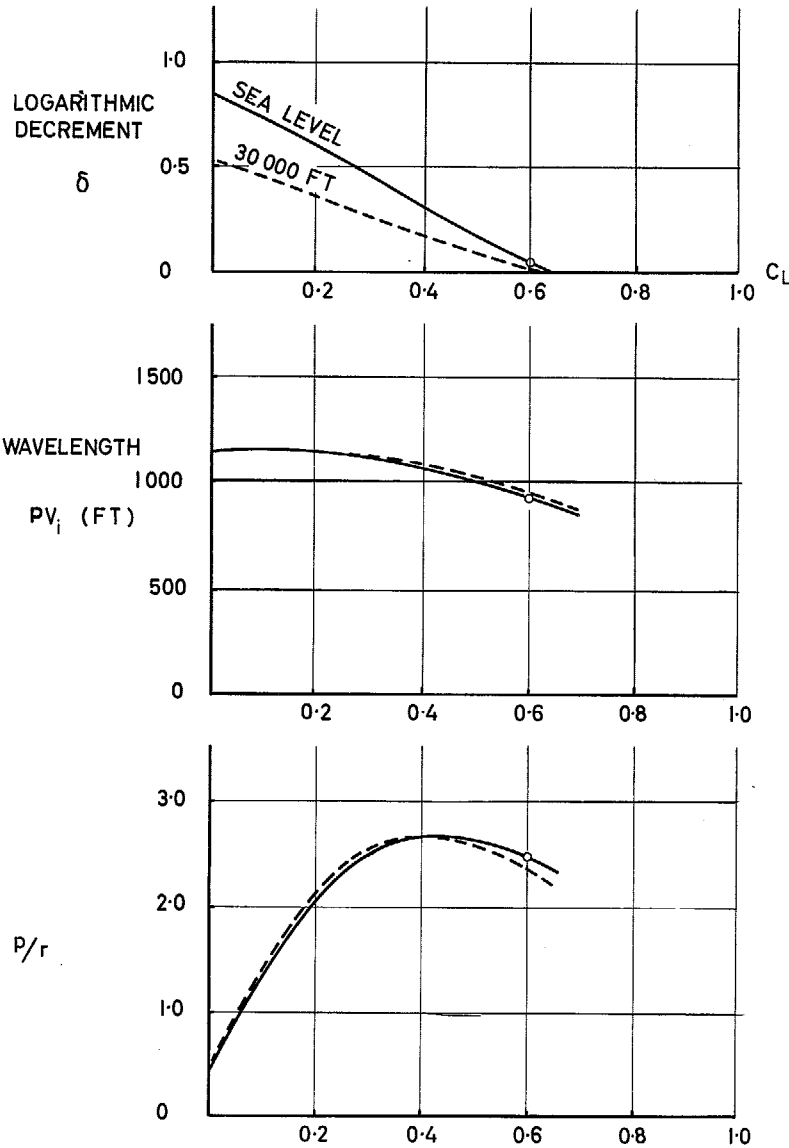
FIG. 16.  Delta-wing aircraft ($A.R. = 1\cdot8$), lateral
stability characteristics.
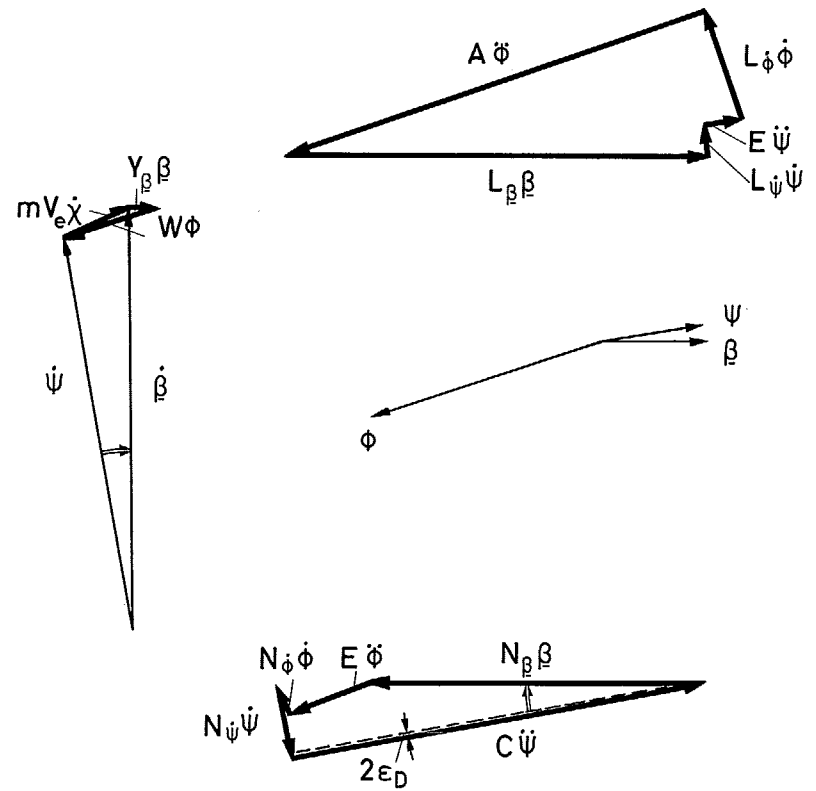


FIG. 17.  Delta-wing aircraft ($A.R. = 1\cdot8$), vector
diagrams. $C_L = 0\cdot6$, sea level.
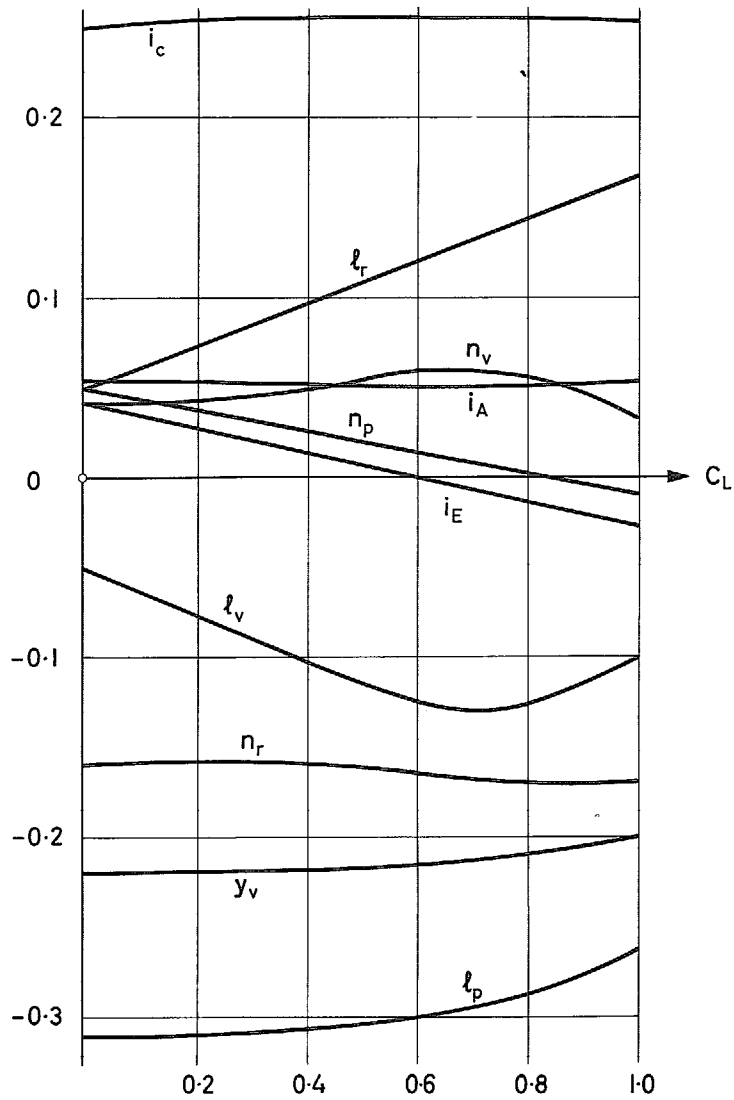
FIG. 18.  Swept-wing aircraft, lateral derivatives.



FIG. 19.  Swept-wing aircraft. Lateral stability characteristics.

(a) $C_L = 0.3$, sea level

(b) $C_L = 1.0$, sea level
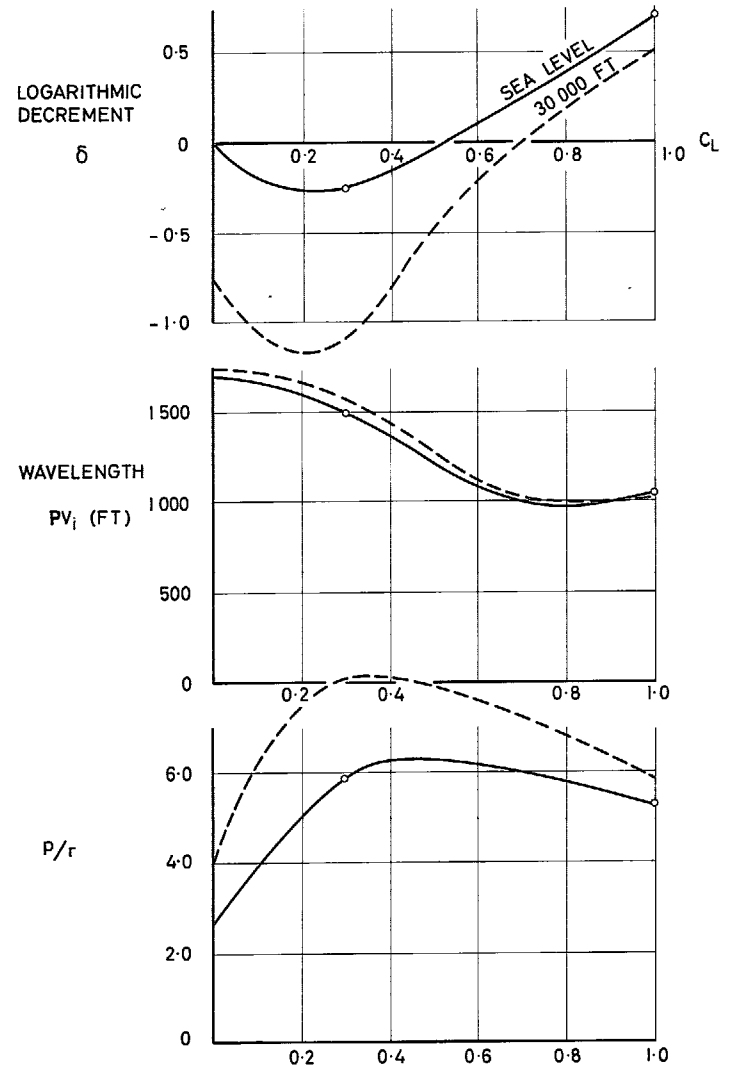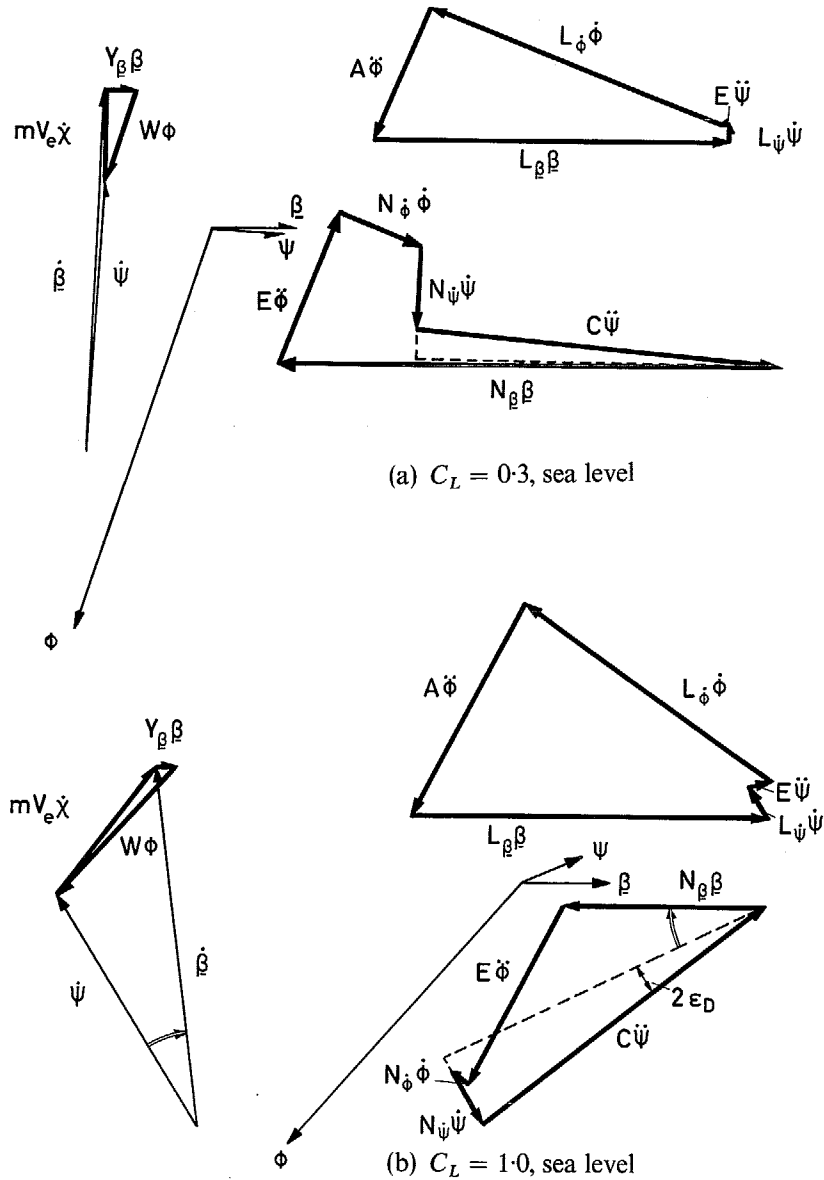
FIG. 20 a & b.    Swept-wing aircraft, vector diagrams.
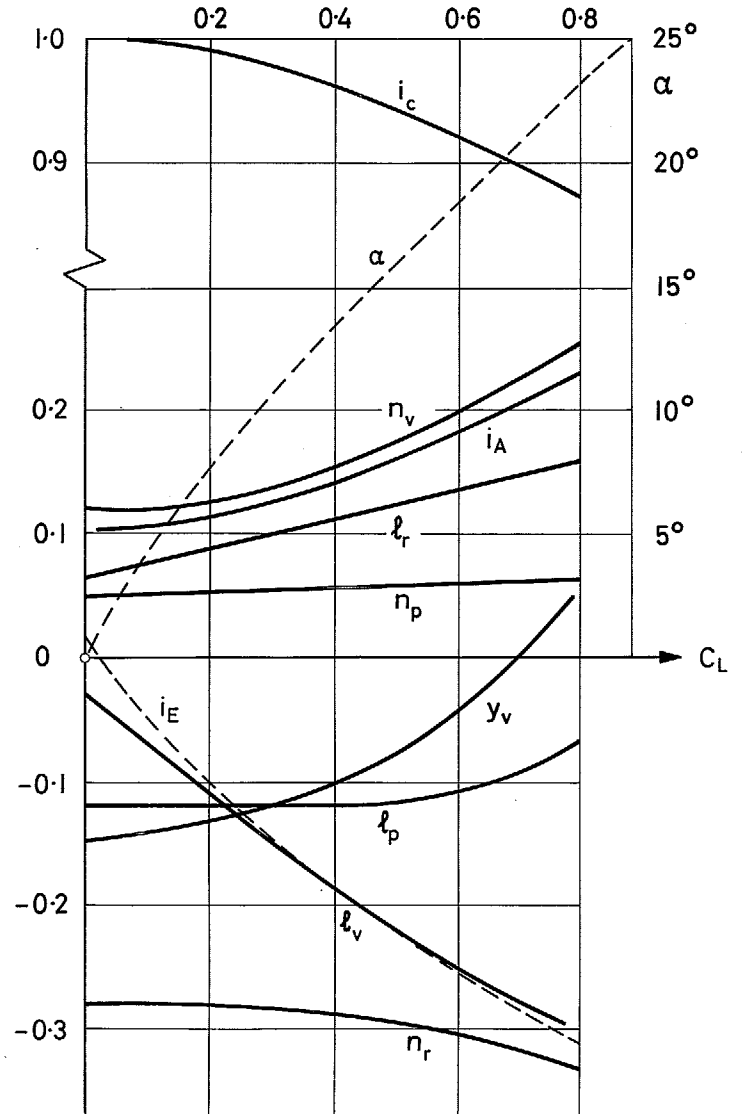


FIG. 21.    Slender-wing aircraft ($A.R. = 1.0$), lateral derivatives.
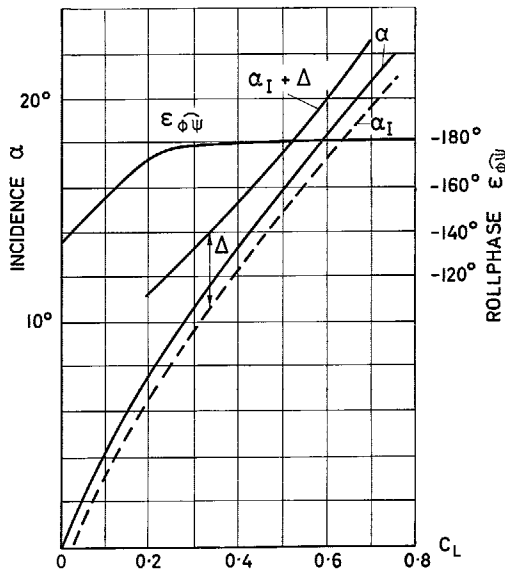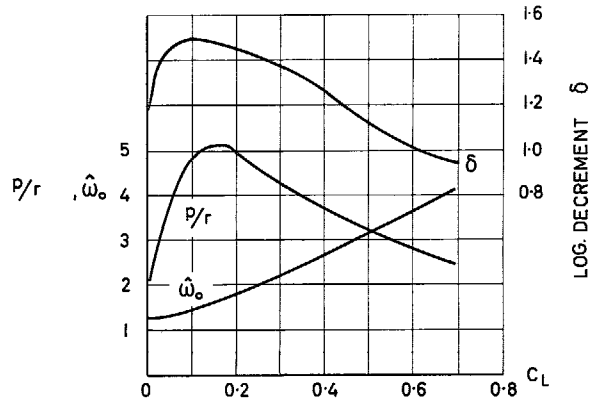
$\Delta$ = ELEVATION OF ROLL AXIS AGAINST PRINCIPAL X - AXIS

$\alpha_I$ = INCIDENCE OF PRINCIPAL X - AXIS

$\propto$ = INCIDENCE OF BODY DATUM LINE

FIG. 22.   Slender-wing aircraft $(A.R. = 1 \cdot 0)$, lateral
oscillation characteristics.
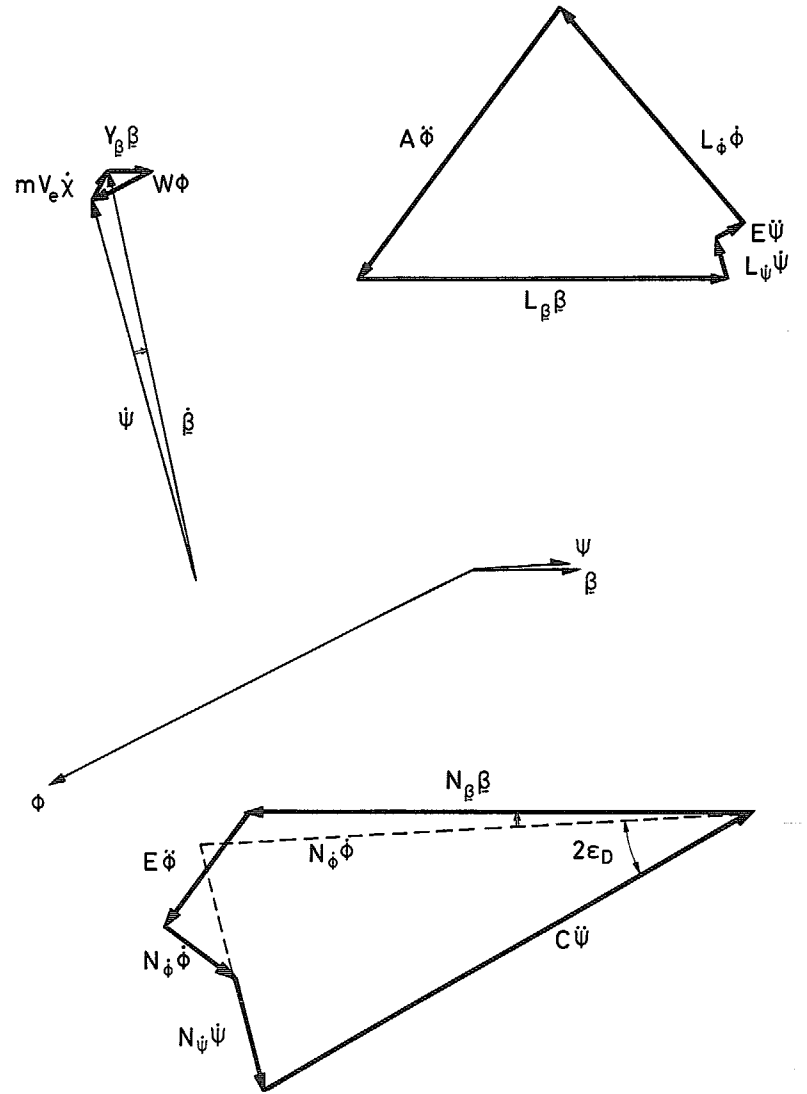


FIG. 23a.   Slender-wing aircraft $(A.R. = 1 \cdot 0)$,
vector diagrams, $C_L = 0 \cdot 1$.
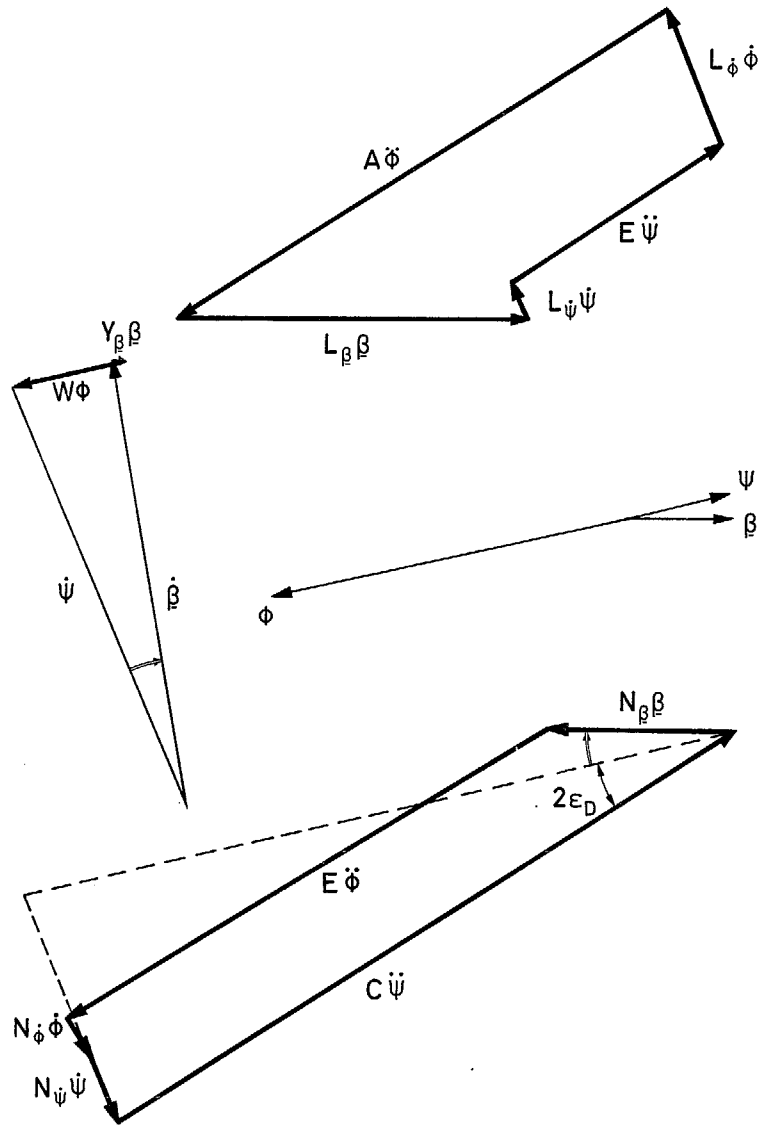
FIG. 23b. Slender-wing aircraft $(A.R. = 1\cdot 0)$, vector diagrams, $C_L = 0\cdot 5$.
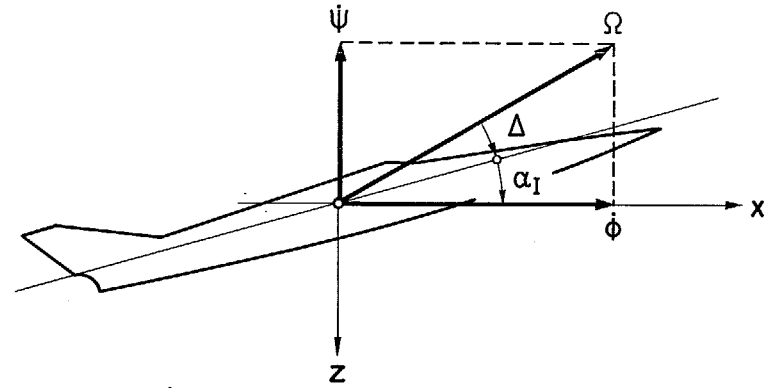
$\alpha_I$ = INCIDENCE OF PRINCIPAL AXIS OF INERTIA

$\Delta$ IS SHOWN MUCH EXAGGERATED

FIG. 24. Slender-wing aircraft, derivation of axis of oscillation.
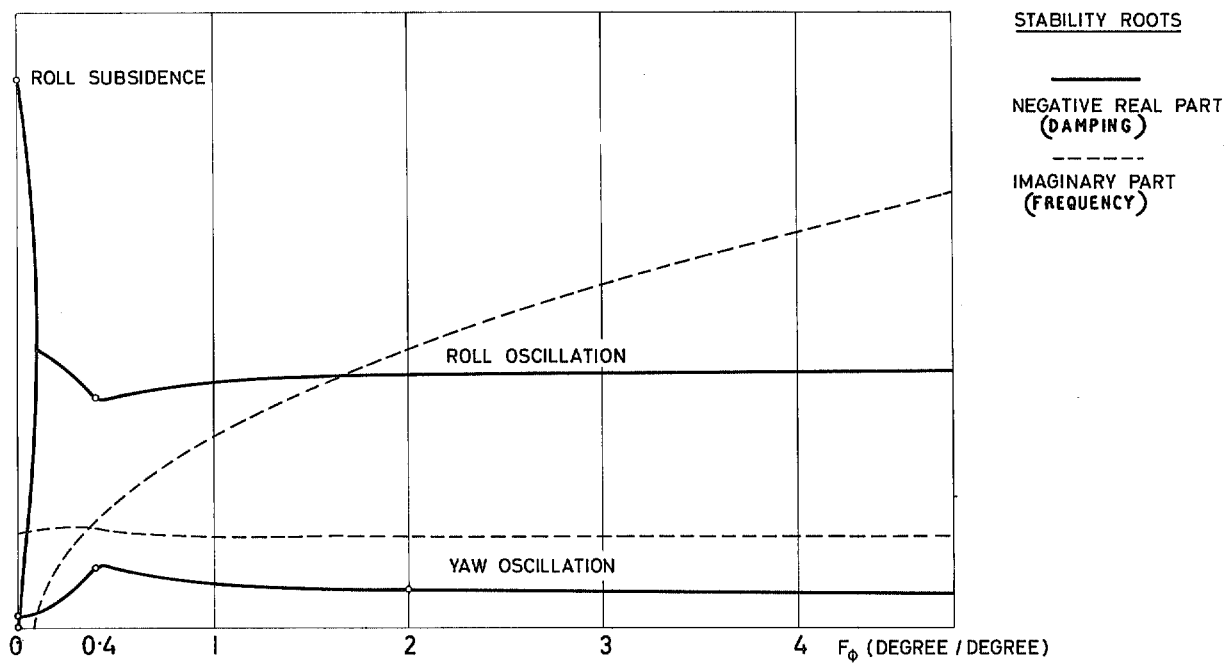
FIG. 25.   Stability diagram, aileron control.
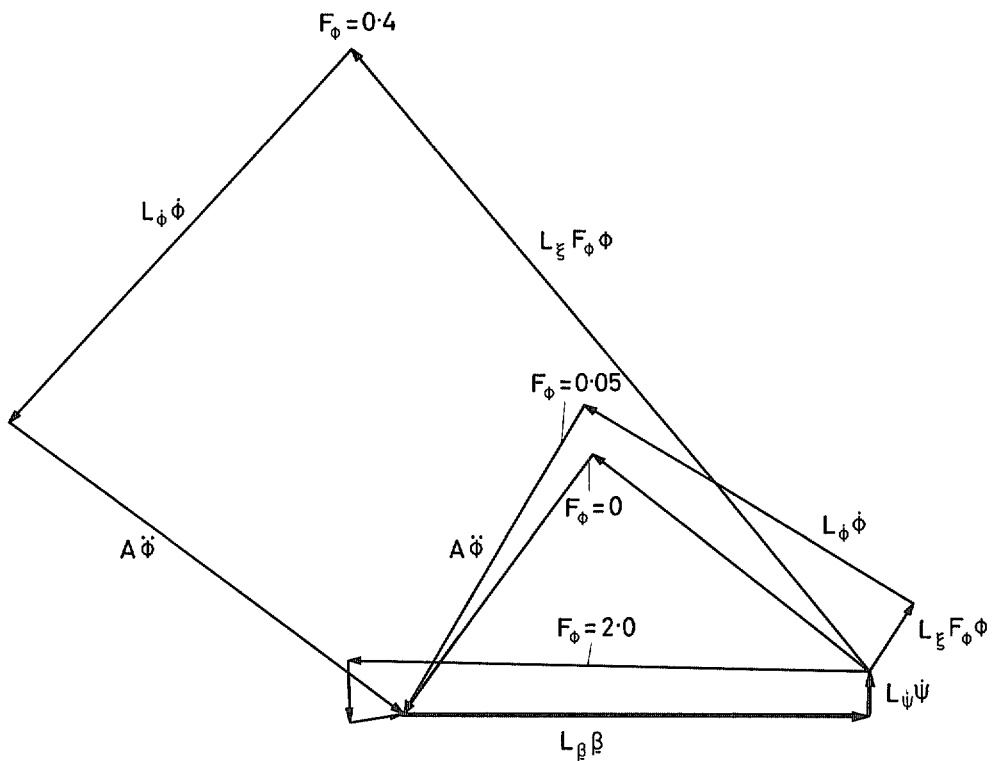


FIG. 26.   Vector diagrams for aileron control, rolling moments.

48
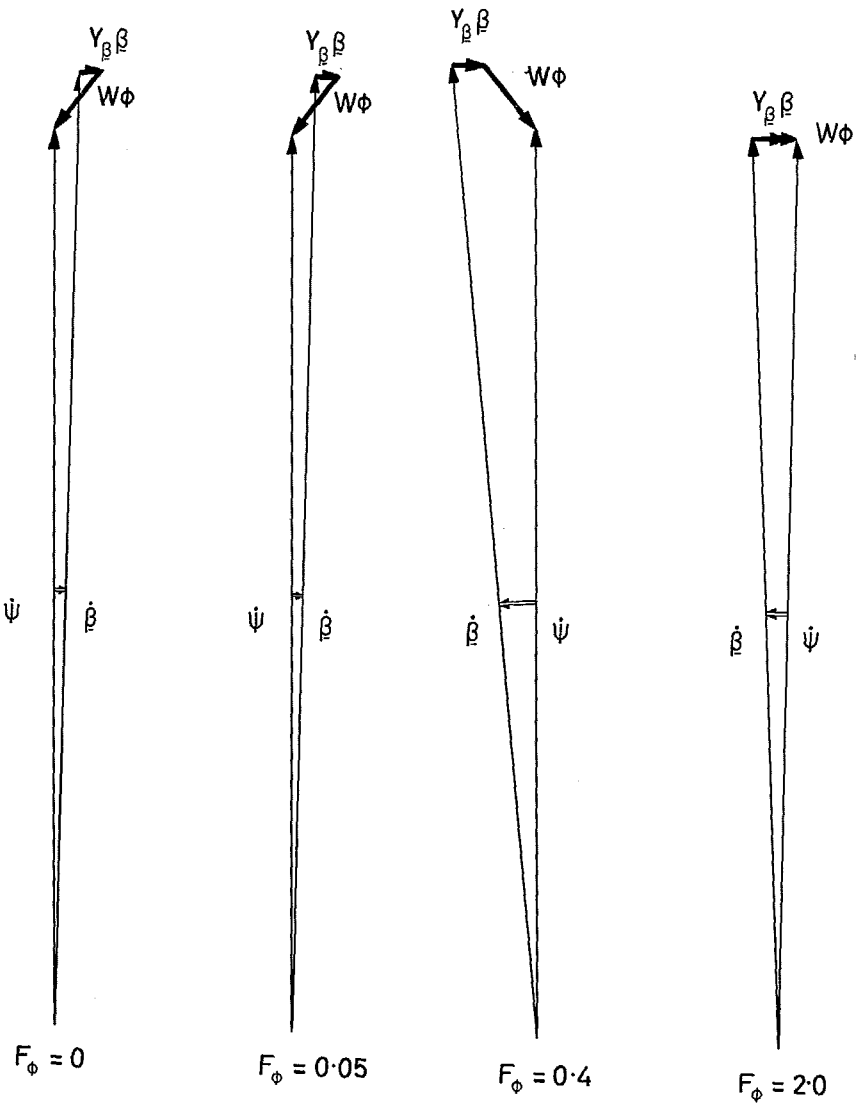
FIG. 27. Vector diagrams for aileron control, sideforces.
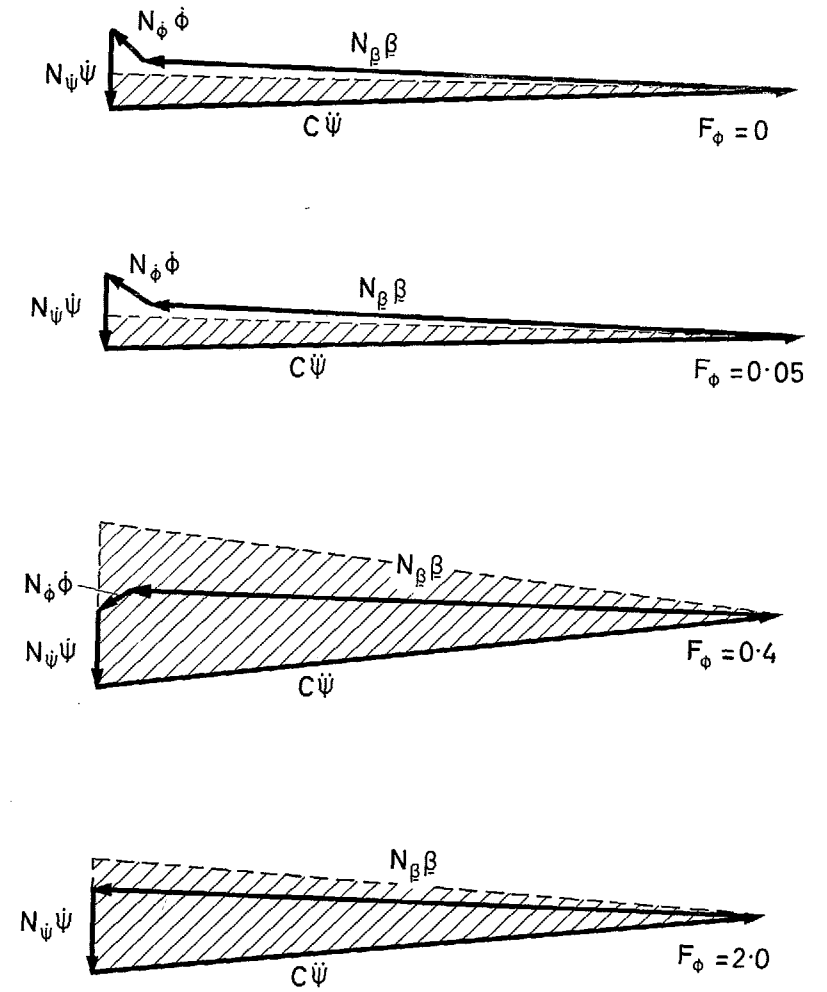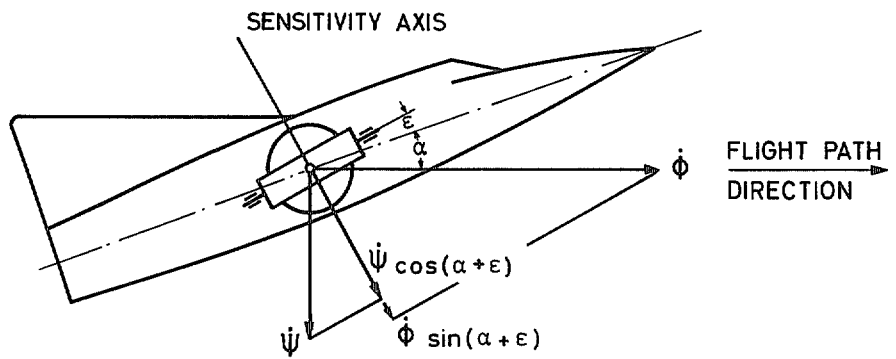
FIG. 28. Vector diagrams for aileron control, yawing moments.

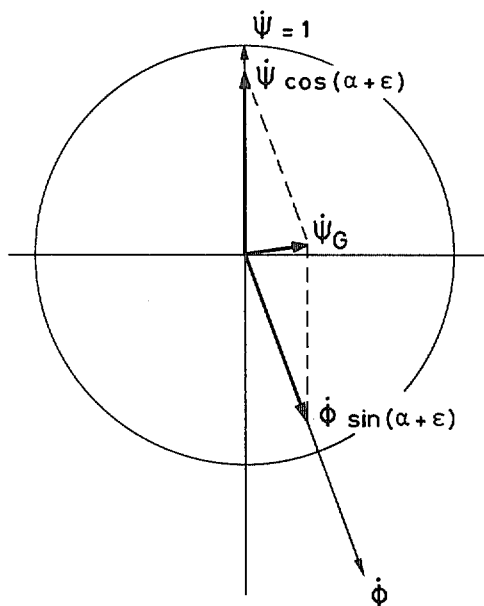**FIG. 29  RATE OF YAW GYRO IN HORIZONTAL FLIGHT**
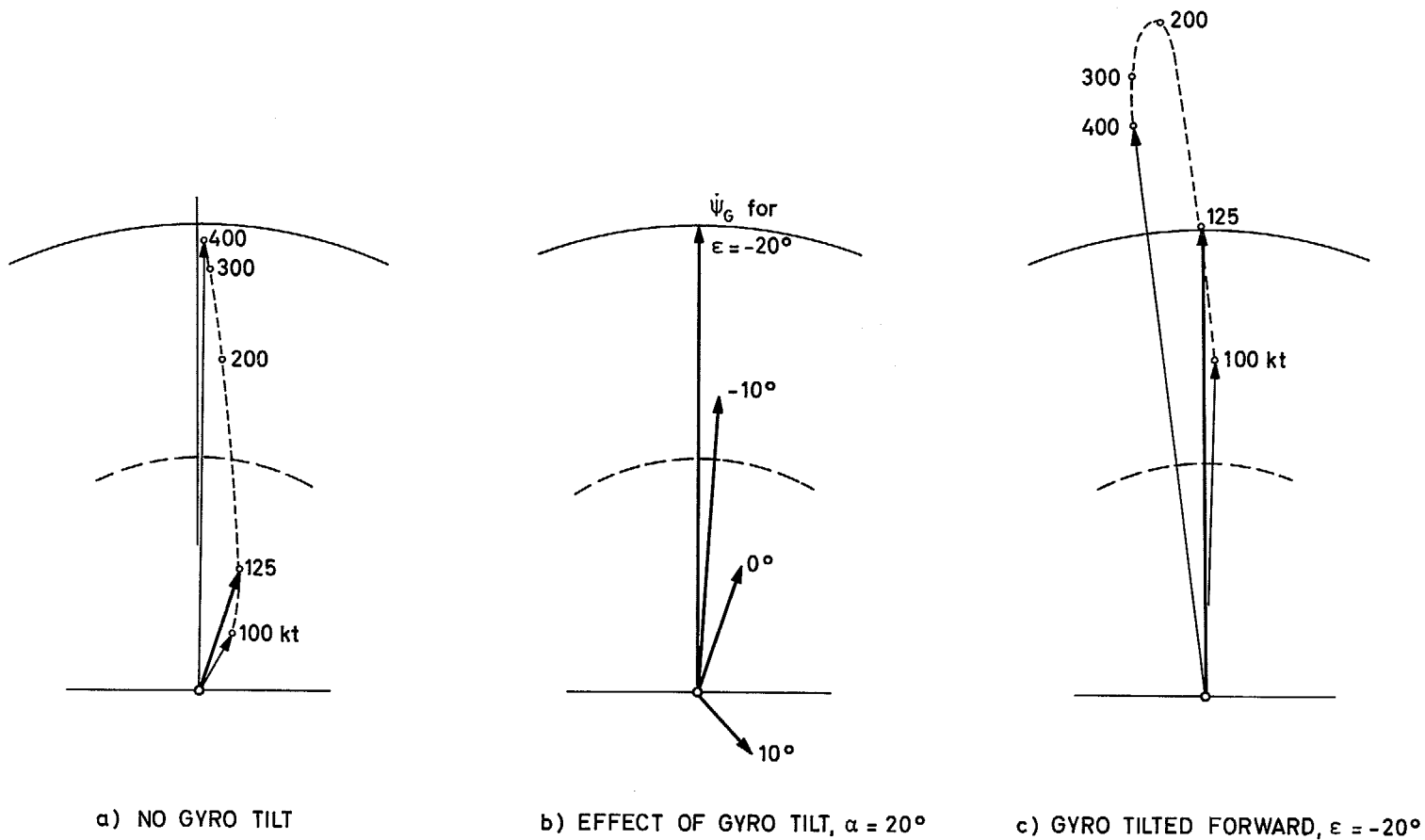


FIG. 30.  Addition of time vectors.

a) NO GYRO TILT

b) EFFECT OF GYRO TILT, α = 20°

c) GYRO TILTED FORWARD, ε = -20°

$\dot{\psi}_G$ for

ε = -20°

Fig. 31.   Time vectors of rate-of-yaw gyro signals.